

Comparison of the lattice Boltzmann equation and discrete unified gas-kinetic scheme methods for direct numerical simulation of decaying turbulent flows

Peng Wang,¹ Lian-Ping Wang,^{1,2} and Zhaoli Guo^{1,*}

¹State Key Laboratory of Coal Combustion, Huazhong University of Science and Technology, Wuhan 430074, China

²Department of Mechanical Engineering, University of Delaware, Newark, Delaware 19716, USA

(Received 17 December 2015; published 13 October 2016)

The main objective of this work is to perform a detailed comparison of the lattice Boltzmann equation (LBE) and the recently developed discrete unified gas-kinetic scheme (DUGKS) methods for direct numerical simulation (DNS) of the decaying homogeneous isotropic turbulence and the Kida vortex flow in a periodic box. The flow fields and key statistical quantities computed by both methods are compared with those from the pseudospectral method at both low and moderate Reynolds numbers. The results show that the LBE is more accurate and efficient than the DUGKS, but the latter has a superior numerical stability, particularly for high Reynolds number flows. In addition, we conclude that the DUGKS can adequately resolve the flow when the minimum spatial resolution parameter $k_{\max}\eta > 3$, where k_{\max} is the maximum resolved wave number and η is the flow Kolmogorov length. This resolution requirement can be contrasted with the requirements of $k_{\max}\eta > 1$ for the pseudospectral method and $k_{\max}\eta > 2$ for the LBE. It should be emphasized that although more validations should be conducted before the DUGKS can be called a viable tool for DNS of turbulent flows, the present work contributes to the overall assessment of the DUGKS, and it provides a basis for further applications of DUGKS in studying the physics of turbulent flows.

DOI: [10.1103/PhysRevE.94.043304](https://doi.org/10.1103/PhysRevE.94.043304)

I. INTRODUCTION

In the study of turbulent flows, the ultimate objective is to obtain accurate coarse-grained quantitative theories or models. However, more than a century's experience has shown this to be notoriously difficult [1]. Fortunately, the ever-increasing power of computers makes it possible to calculate relevant properties of turbulent flows by direct numerical simulation (DNS). Significant insight into turbulence physics has been gained from the DNS of some idealized flows that cannot be easily obtained in the laboratory [2–4]. The conventional DNS is based on the Navier-Stokes equations (NSEs), which are a set of second-order nonlinear partial-differential equations (PDEs). However, it is usually involute and computationally expensive to deal with the nonlinear and nonlocal convection term and pressure-gradient term in the NSEs [1]. Therefore, it is desirable to find an alternative numerical method for DNS that not only can accurately capture all the scales of turbulence, but is simpler and more efficient. Recently, Boltzmann-equation-based kinetic schemes have received particular attention as alternative solutions to the NSEs due to some distinctive features. Different from the NSEs, the Boltzmann equation is a first-order linear PDE, and the nonlinearity resides locally in its collision term; both make such schemes easy to realize and parallelize to have a high computational efficiency. It has been argued that the kinetic equation with local nonlinearity is more feasible to handle the discontinuities or unresolved flow regions [5]. Furthermore, the Boltzmann equation provides a theoretical foundation for the hydrodynamic description from the underlying microscopic physics, and it describes the phenomenon of fluid flows in the statistical mechanics framework. This physical mechanism is inherently consistent

with the physical process of turbulent flows, which are characterized by their statistical behavior [6]. Therefore, the kinetic schemes based on the Boltzmann equation have a great potential for DNS of turbulent flows [7].

In recent years, some kinetic schemes have been utilized to simulate turbulent flows, such as the lattice Boltzmann equation (LBE) methods [8–22] and the gas-kinetic schemes [23–27]. In particular, the LBE methods have been successfully applied to complex and multiscale flows due to their simplicity in formulation and versatility [28–31]. The potential of the LBE methods for DNS of turbulent flows was demonstrated shortly after their emergence by comparing with pseudospectral (PS) simulations of decaying homogeneous isotropic turbulence (DHIT) [8,9] and turbulence shear flows [10,11]. An appealing feature of the LBE methods in turbulence simulations, as a scheme of second-order spatial accuracy, is that it has very low numerical dissipation compared to the second-order conventional computational fluids dynamics (CFD) methods [32]. It has been demonstrated that the larger numerical dissipation in second-order accurate conventional CFD translates into greater resolution requirements [3].

Recently, starting from the Boltzmann equation, a discrete unified gas-kinetic scheme (DUGKS) was proposed for flows in all Knudsen regimes [33,34]. Although they share a common kinetic origin, there are some distinctive differences between the DUGKS and LBE methods. In the standard LBE, the phase space and time step are coupled due to the particle motion from one node to another within a time step [31], but the DUGKS has no such restriction, and the time step is determined independently by the Courant-Friedrichs-Lewy (CFL) condition [33]. In addition, the streaming process in the LBE makes it difficult to extend to nonuniform mesh, while the DUGKS can use arbitrary meshes [35]. Although some efforts have been made to release the close coupling between the mesh and discrete velocities [36–42], the decoupling also destroys

*zlguo@hust.edu.cn

the nice features of the standard LBE. For example, many of the existing finite volume (FV) LBE methods suffer from large numerical dissipation and poor numerical stability [40,41]. More importantly, there are modeling differences in the LBE and DUGKS in the treatment of particle evolution. In the LBE, the particle streaming and collision processes are split. However, these two processes are fully coupled in DUGKS. It has been demonstrated that such a strategy ensures a low numerical dissipation feature [43,44]. It should be noted that although in some cases a finite-volume scheme can be identical to a finite-difference scheme, the DUGKS does not reduce to the standard LBE method generally, because the shift (streaming) operation in the LBE cannot be realized for some discrete populations in the FV framework (e.g., the diagonal populations in the D2Q9 model). Furthermore, in DUGKS the flux is evaluated by solving the evolution equation rather than interpolation. Therefore, the DUGKS would not be identical to the LBE. Consequently, these dynamic differences between the LBE and DUGKS methods determine the quality of solution in flow simulations. A comparative study of the LBE and DUGKS methods for laminar flows in the nearly incompressible limit was performed recently [45]. It demonstrated that the DUGKS has the same accuracy as the LBE, but it exhibits a superior numerical stability. The superiority of the DUGKS compared to the LBE methods for laminar flows motivates us to perform an additional comparative study of DUGKS and LBE methods for turbulent flows.

Our long-term goal concentrates on providing some insights into the physics of complex turbulent flows by using DUGKS as a DNS tool. At a first step, the validation of the DUGKS for simulating simple turbulent flows must be undertaken. The DHIT is one such basic flow in turbulence study, and also a canonical case to validate a numerical scheme for DNS of turbulent flows. The objective of this work is to make a detailed comparison of the LBE and DUGKS methods by simulating the decaying turbulent flows in a periodic box. To date, the PS method is well-established as the most accurate numerical tool for DNS of the DHIT. Therefore, the DUGKS numerical results will be validated against those from the PS method. In addition, we use the LBE with the multiple relaxation time (MRT-LBE) collision model in this work due to its superiority over the single relaxation collision model [45]. The comparative study covers the following aspects of the simulated flows: (i) the instantaneous velocity and vorticity fields; (ii) the evolutions of kinetic energy, dissipation rate, and enstrophy; (iii) the energy and the dissipation rate spectra; (iv) the evolutions of the Kolmogorov length scale and the Taylor microscale length; and (v) the evolutions of the averaged velocity-derivative skewness and flatness. Furthermore, DNS of the Kida flow is also performed by the LBE and DUGKS methods, and some comparisons are performed in terms of the vorticity, evolutions of the total kinetic energy, dissipation rate, enstrophy and Kolmogorov length scale, the longitudinal and transverse correlations, and the pressure-velocity correlations.

The remainder of this paper is organized as follows: in Sec. II, we provide a brief introduction of the DUGKS and MRT-LBE methods; Sec. III introduces the DHIT and Kida vortex flow, and the quantities to be computed; Sec. IV presents the numerical results followed by a summary of conclusions.

II. NUMERICAL METHODS

In this section, the essentials of DUGKS and the LBE with multiple-relaxation time collision model (MRT-LBE) will be introduced briefly first. A more detailed description can be found in Refs. [13,33].

A. The DUGKS method

The DUGKS is based on the BGK collision model [46], which begins with the model Boltzmann equation,

$$\frac{\partial f}{\partial t} + \boldsymbol{\xi} \cdot \nabla_{\mathbf{x}} f = \Omega \equiv \frac{f^{\text{eq}} - f}{\tau}, \quad (1)$$

where $f = f(\mathbf{x}, \boldsymbol{\xi}, t)$ is the particle distribution function with particle velocity $\boldsymbol{\xi}$ at position \mathbf{x} and time t , and f^{eq} is the Maxwellian equilibrium distribution function,

$$f^{\text{eq}} = \frac{\rho}{(2\pi RT)^{D/2}} \exp\left(-\frac{(\boldsymbol{\xi} - \mathbf{u})^2}{2RT}\right), \quad (2)$$

where R is the gas constant, D is the spatial dimension, ρ is the density, \mathbf{u} is the fluid velocity, and T is the temperature. It should be noted that the dimensions of f and f^{eq} are both $kg/[m^D(m/s)^D]$. For incompressible flow (i.e., when the Mach number Ma is small), the Maxwellian distribution can be approximated by its Taylor expansion around zero particle velocity. As a result, the expanded equilibrium distribution function becomes

$$f^{\text{eq}} = \frac{\rho}{(2\pi RT)^{D/2}} \exp\left(-\frac{|\boldsymbol{\xi}|^2}{2RT}\right) \left[1 + \frac{\boldsymbol{\xi} \cdot \mathbf{u}}{RT} + \frac{(\boldsymbol{\xi} \cdot \mathbf{u})^2}{2(RT)^2} - \frac{|\mathbf{u}|^2}{2RT}\right]. \quad (3)$$

To obtain the correct NSEs in the limit of low Mach number, the discrete velocity set should be chosen so that the following quadratures of the expanded equilibrium distribution function hold exactly:

$$\int \boldsymbol{\xi}^k f^{\text{eq}} d\boldsymbol{\xi} = \sum_i \omega_i \boldsymbol{\xi}_i^k f^{\text{eq}}(\boldsymbol{\xi}_i), \quad 0 \leq k \leq 3, \quad (4)$$

where ω_i and $\boldsymbol{\xi}_i$ are the weights and points of the numerical quadrature rule. Based on the formulation of Eq. (3), it is natural to choose a Gaussian quadrature with $\omega_i = W_i (2\pi RT)^{D/2} \exp(-\frac{|\boldsymbol{\xi}_i|^2}{2RT})$, in which W_i is the weight coefficient corresponding to the particle velocity $\boldsymbol{\xi}_i$.

In the present study, we use the 19 velocities in three dimensions, i.e., the D3Q19 model, for both the DUGKS and LBE, where

$$\boldsymbol{\xi}_i = \begin{cases} (0, 0), & i = 0, \\ (\pm 1, 0, 0)c, (0, \pm 1, 0)c, (0, 0, \pm 1)c, & i = 1 - 6, \\ (\pm 1, \pm 1, 0)c, (\pm 1, 0, \pm 1)c, (0, \pm 1, \pm 1)c, & i = 7 - 18, \end{cases} \quad (5)$$

where $c = \sqrt{3RT}$, and the corresponding weight coefficients are $W_0 = 1/3$, $W_{1,\dots,6} = 1/18$, and $W_{7,\dots,18} = 1/36$.

Once the quadrature rule is chosen, we can define a discrete distribution function, $f_i(\mathbf{x}, t) = \omega_i f(\mathbf{x}, \boldsymbol{\xi}_i, t)$, which satisfies the following equation:

$$\frac{\partial f_i}{\partial t} + \boldsymbol{\xi}_i \cdot \nabla_{\mathbf{x}} f_i = \Omega_i \equiv \frac{f_i^{\text{eq}} - f_i}{\tau}, \quad (6)$$

where $f_i^{\text{eq}} = \omega_i f^{\text{eq}}(\boldsymbol{\xi}_i)$ is the discrete expanded equilibrium distribution function that can be written as

$$f_i^{\text{eq}} = W_i \left[\delta\rho + \rho_0 \left(\frac{\boldsymbol{\xi}_i \cdot \mathbf{u}}{RT} + \frac{(\boldsymbol{\xi}_i \cdot \mathbf{u})^2}{2(RT)^2} - \frac{|\mathbf{u}|^2}{2RT} \right) \right], \quad (7)$$

where the density has been expressed as $\rho = \delta\rho + \rho_0$, in which $\delta\rho$ is the density fluctuation, and ρ_0 is the constant mean density of the fluid, which is usually set to be 1. It should be emphasized that with the discrete velocity set, the dimensions of f_i and f_i^{eq} are both kg/m^D . Then, the fluid density and velocity can be obtained from the discrete distribution function,

$$\rho = \rho_0 + \delta\rho, \quad \delta\rho = \sum_i f_i, \quad \rho_0 \mathbf{u} = \sum_i \boldsymbol{\xi}_i f_i. \quad (8)$$

The DUGKS is a finite-volume scheme in which the computational domain is divided into a set of control volumes. Then integrating Eq. (6) over a control volume V_j centered at \mathbf{x}_j from t_n to t_{n+1} (the time step $\Delta t = t_{n+1} - t_n$ is assumed to be a constant in the present work), and using the midpoint rule for the integration of the flux term at the cell boundary and trapezoidal rule for the collision term inside each cell [33], we can get the evolution equation of DUGKS,

$$\tilde{f}_{i,j}^{n+1} = \tilde{f}_{i,j}^{+,n} - \frac{\Delta t}{|V_j|} F_i^{n+1/2}, \quad (9)$$

where

$$F_i^{n+1/2} = \int_{\partial V_j} (\boldsymbol{\xi}_i \cdot \mathbf{n}) f_i(\mathbf{x}, t_{n+1/2}) dS \quad (10)$$

is the flux across the cell interface, and

$$\tilde{f}_i = f_i - \frac{\Delta t}{2} \Omega_i, \quad \tilde{f}_i^+ = f_i + \frac{\Delta t}{2} \Omega_i. \quad (11)$$

Based on the compatibility condition and the relationship between f_i and \tilde{f}_i , the density ρ and velocity \mathbf{u} can be computed by

$$\rho = \rho_0 + \delta\rho, \quad \delta\rho = \sum_i \tilde{f}_i, \quad \rho_0 \mathbf{u} = \sum_i \boldsymbol{\xi}_i \tilde{f}_i. \quad (12)$$

The key ingredient in updating \tilde{f}_i is to evaluate the interface flux $F_i^{n+1/2}$, which is solely determined by the distribution function $f_i(\mathbf{x}, t_{n+1/2})$ there. In DUGKS, after integrating Eq. (6) along a particle path within a half time step ($h = \Delta t/2$), the evaluation of the distribution function $f_i(\mathbf{x}, t_{n+1/2})$ at the cell interface can be traced back to the interior of neighboring cells,

$$\tilde{f}_i(\mathbf{x}_b, t_n + h) = \tilde{f}_i^+(\mathbf{x}_b, t_n) - h \boldsymbol{\xi}_i \cdot \boldsymbol{\sigma}_b, \quad (13)$$

where

$$\tilde{f}_i = f_i - \frac{h}{2} \Omega_i, \quad \tilde{f}_i^+ = f_i + \frac{h}{2} \Omega_i, \quad (14)$$

$\tilde{f}_i^+(\mathbf{x}_b, t_n)$ and the gradient $\boldsymbol{\sigma}_b = \nabla \tilde{f}_i^+(\mathbf{x}_b, t_n)$ can be approximated by linear interpolation. For example, in the one-dimensional case, the reconstructions become

$$\tilde{f}_i^+(x_{j+1/2}, t_n) = \tilde{f}_i^+(x_j, t_n) + \sigma_{j+1/2}(x_{j+1/2} - x_j), \quad (15)$$

where

$$\sigma_{j+1/2} = \frac{\tilde{f}_i^+(x_{j+1}, t_n) - \tilde{f}_i^+(x_j, t_n)}{x_{j+1} - x_j}. \quad (16)$$

Note that the particle collision effect from t_n to t_{n+1} is included in the above reconstruction of the interface distribution function. This is the key for the success of the DUGKS. Due to the coupled treatment of the particle collision and transport process in the reconstruction of the distribution function at cell interfaces, DUGKS is a self-adaptive scheme for different flow regimes. It has been shown in Ref. [33] that the reconstructed distribution function reduces to the Chapman-Enskog approximation at the Navier-Stokes level in the continuum limit, and to the free-transport approximation in the free-molecular limit.

Based on the compatibility condition and the relationship between f_i and \tilde{f}_i , the density ρ and velocity \mathbf{u} at the cell interface can be obtained,

$$\rho = \rho_0 + \delta\rho, \quad \delta\rho = \sum_i \tilde{f}_i, \quad \rho_0 \mathbf{u} = \sum_i \boldsymbol{\xi}_i \tilde{f}_i \quad (17)$$

from which the equilibrium distribution function $f_i^{\text{eq}}(\mathbf{x}_b, t^n + h)$ at the cell interface can be obtained. Therefore, based on Eq. (14) and the obtained equilibrium state, the real distribution function at the cell interface can be determined from \tilde{f}_i as

$$f_i(\mathbf{x}_b, t_n + h) = \frac{2\tau}{2\tau + h} \tilde{f}_i(\mathbf{x}_b, t_n + h) + \frac{h}{2\tau + h} f_i^{\text{eq}}(\mathbf{x}_b, t_n + h), \quad (18)$$

from which the interface flux term can be evaluated.

In computation, we only need to follow the evolution of \tilde{f}_i in Eq. (9). The required variables for its evolution are determined by [33]

$$\tilde{f}_i^+ = \frac{2\tau - h}{2\tau + \Delta t} \tilde{f}_i + \frac{3h}{2\tau + \Delta t} f_i^{\text{eq}}, \quad (19)$$

$$\tilde{f}_i^+ = \frac{4}{3} \tilde{f}_i^+ - \frac{1}{3} \tilde{f}_i. \quad (20)$$

B. The MRT-LBE method

In this work, we use the LBE with multiple-relaxation time collision model (MRT-LBE) and the D3Q19 discrete velocity sets. The evolution equation of the MRT-LBE is

$$\mathbf{f}(\mathbf{x} + \boldsymbol{\xi}_i \Delta t, t_n + \Delta t) = \mathbf{f}(\mathbf{x}, t_n) - \mathbf{M}^{-1} \mathbf{S} [\mathbf{m}(\mathbf{x}, t) - \mathbf{m}^{\text{eq}}(\mathbf{x}, t)], \quad (21)$$

where \mathbf{M} is an orthogonal transformation matrix converting the distribution function \mathbf{f} from discrete velocity space to the moment space \mathbf{m} , in which the collision relaxation is performed.

The basic idea of MRT-LBE is that the streaming substep is handled in the microscopic lattice-velocity space, but the collision substep is performed in the moment space. The

transformation between the microscopic velocity space and the moment space is carried out by matrix operations as $\mathbf{m} = \mathbf{M} \cdot \mathbf{f}$, $\mathbf{f} = \mathbf{M}^{-1} \cdot \mathbf{m}$. The diagonal relaxation matrix \mathbf{S} specifies the relaxation rates for the nonconserved moments.

The macroscopic hydrodynamic variables, including the density ρ and momentum, are obtained from the moments of the mesoscopic distribution function \mathbf{f} . In the nearly incompressible formulation [47],

$$\rho = \rho_0 + \delta\rho, \quad \rho_0 = 1; \quad \delta\rho = \sum_i f_i, \quad \rho_0 \mathbf{u} = (j_x, j_y, j_z)^T = \sum_i \xi_i f_i. \quad (22)$$

For the D3Q19 velocity model, the corresponding 19 orthogonal moments

$$\mathbf{m} = (\delta\rho, e, \varepsilon, j_x, q_x, j_y, q_y, j_z, q_z, 3p_{xx}, 3\pi_{xx}, p_{ww}, \pi_{ww}, p_{xy}, p_{yz}, p_{xz}, m_x, m_y, m_z)^T$$

are defined through the element of the transformation matrix (each subscript runs from 0 to 18) as

$$\begin{aligned} M_{0,\alpha} &= \|\xi_\alpha\|^0, & M_{1,\alpha} &= 19\|\xi_\alpha\|^2 - 30, & M_{2,\alpha} &= (21\|\xi_\alpha\|^4 - 53\|\xi_\alpha\|^2 + 24)/2, \\ M_{3,\alpha} &= \xi_{\alpha x}, & M_{5,\alpha} &= \xi_{\alpha y}, & M_{7,\alpha} &= \xi_{\alpha z}, \\ M_{4,\alpha} &= (5\|\xi_\alpha\|^2 - 9)\xi_{\alpha x}, & M_{6,\alpha} &= (5\|\xi_\alpha\|^2 - 9)\xi_{\alpha y}, & M_{8,\alpha} &= (5\|\xi_\alpha\|^2 - 9)\xi_{\alpha z}, \\ M_{9,\alpha} &= 3\xi_{\alpha x}^2 - \|\xi_\alpha\|^2, & M_{11,\alpha} &= \xi_{\alpha y}^2 - \xi_{\alpha z}^2, \\ M_{13,\alpha} &= \xi_{\alpha x}\xi_{\alpha y}, & M_{14,\alpha} &= \xi_{\alpha y}\xi_{\alpha z}, & M_{15,\alpha} &= \xi_{\alpha x}\xi_{\alpha z}, \\ M_{10,\alpha} &= (3\|\xi_\alpha\|^2 - 5)(3\xi_{\alpha x}^2 - \|\xi_\alpha\|^2), & M_{12,\alpha} &= (3\|\xi_\alpha\|^2 - 5)(\xi_{\alpha y}^2 - \xi_{\alpha z}^2), \\ M_{16,\alpha} &= (\xi_{\alpha y}^2 - \xi_{\alpha z}^2)\xi_{\alpha x}, & M_{17,\alpha} &= (\xi_{\alpha z}^2 - \xi_{\alpha x}^2)\xi_{\alpha y}, & M_{18,\alpha} &= (\xi_{\alpha x}^2 - \xi_{\alpha y}^2)\xi_{\alpha z}. \end{aligned}$$

The equilibrium moments are defined as

$$\begin{aligned} \tilde{\rho}^{(\text{eq})} &= \tilde{\rho} = \delta\rho, & e^{(\text{eq})} &= -11\delta\rho + \frac{19}{\rho_0}(j_x^2 + j_y^2 + j_z^2), & \varepsilon^{(\text{eq})} &= \omega_\varepsilon\delta\rho + \frac{\omega_{\varepsilon j}}{\rho_0}(j_x^2 + j_y^2 + j_z^2), \\ j_x^{(\text{eq})} &= j_x = \rho_0 u_x, & j_y^{(\text{eq})} &= j_y = \rho_0 u_y, & j_z^{(\text{eq})} &= j_z = \rho_0 u_z, \\ q_x^{(\text{eq})} &= -\frac{2}{3}j_x, & q_y^{(\text{eq})} &= -\frac{2}{3}j_y, & q_z^{(\text{eq})} &= -\frac{2}{3}j_z, \\ p_{xx}^{(\text{eq})} &= \frac{1}{3\rho_0}[2j_x^2 - (j_y^2 + j_z^2)], & p_{ww}^{(\text{eq})} &= \frac{1}{\rho_0}[j_y^2 - j_z^2], \\ p_{xy}^{(\text{eq})} &= \frac{1}{\rho_0}j_x j_y, & p_{yz}^{(\text{eq})} &= \frac{1}{\rho_0}j_y j_z, & p_{xz}^{(\text{eq})} &= \frac{1}{\rho_0}j_x j_z, \\ \pi_{xx}^{(\text{eq})} &= \omega_{xx} p_{xx}^{(\text{eq})}, & \pi_{ww}^{(\text{eq})} &= \omega_{xx} p_{ww}^{(\text{eq})}, \\ m_x^{(\text{eq})} &= m_y^{(\text{eq})} = m_z^{(\text{eq})} = 0, \end{aligned}$$

with the following relaxation parameters:

$$\mathbf{S} = \text{diag}(0, s_1, s_2, 0, s_4, 0, s_4, 0, s_4, s_9, s_{10}, s_9, s_{10}, s_{13}, s_{13}, s_{13}, s_{16}, s_{16}, s_{16}).$$

The kinematic viscosity ν and bulk viscosity ζ are related to the relaxation rates s_9 and s_1 , respectively, where

$$\nu = \frac{1}{3} \left(\frac{1}{s_9} - \frac{1}{2} \right) c \Delta x, \quad (23)$$

$$\zeta = \frac{5 - 9c_s^2}{9} \left(\frac{1}{s_1} - \frac{1}{2} \right) c \Delta x, \quad (24)$$

where $c_s^2 = RT$ is the speed of sound.

It is noted that some of the relaxation parameters do not affect the simulated flow, but they may affect the numerical stability of the code. Specifically, s_1 determines the bulk viscosity, which could absorb low-amplitude acoustic oscillations.

III. DECAYING TURBULENT FLOWS

A. Decaying homogeneous isotropic turbulence

The DHIT in a three-dimensional box with periodic boundary conditions in all three directions is a standard test case to validate the numerical scheme for DNS. At the initial time, a random flow field is introduced with the

TABLE I. Parameters used in the LBE, DUGKS, and PS simulations.

Method	L	N	K_0	u'_0	ν
PS128	2π	128	0.9241	0.7849	1.4933×10^{-2}
LBE128	128	128	1.5383×10^{-3}	0.0320	1.2395×10^{-2}
DUGKS128	128	128	1.5383×10^{-3}	0.0320	1.2395×10^{-2}
PS256	2π	256	0.9241	0.7849	1.4933×10^{-2}
LBE256	256	256	1.5383×10^{-3}	0.0320	2.4790×10^{-2}
DUGKS256	256	256	1.5383×10^{-3}	0.0320	2.4790×10^{-2}

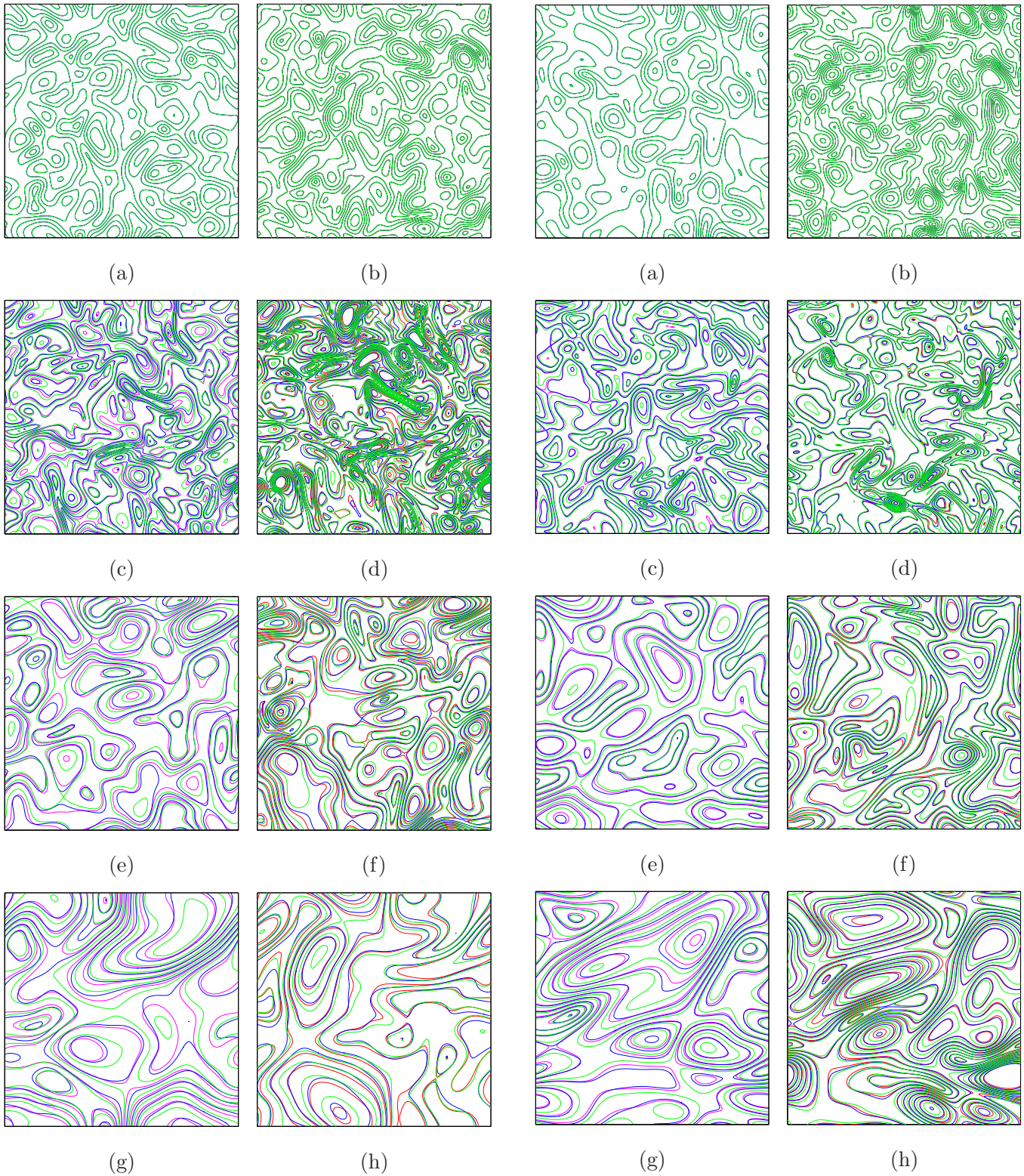
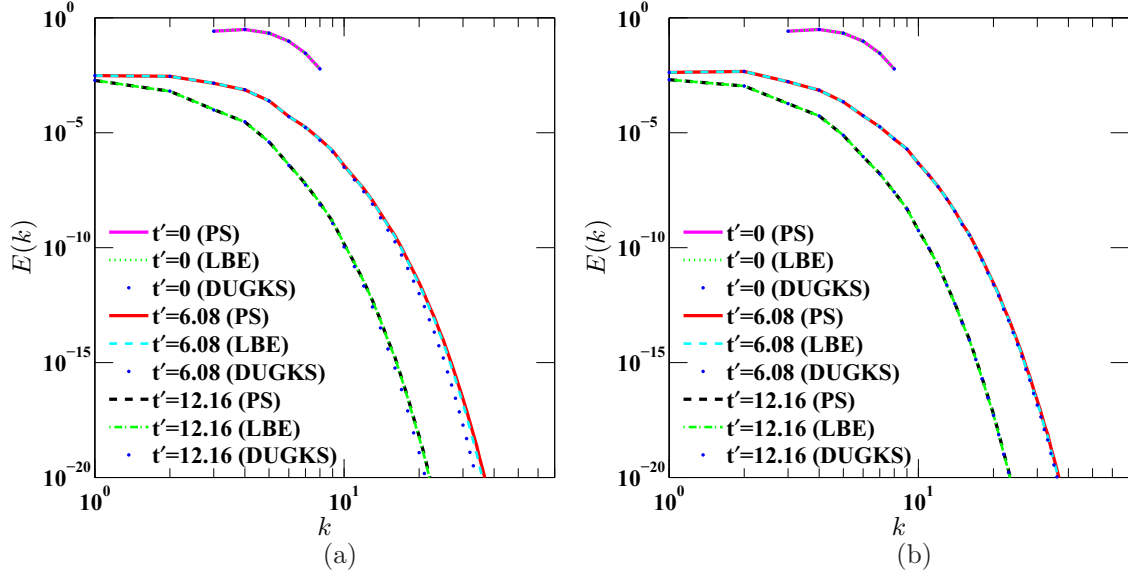


FIG. 1. Contours of normalized velocity magnitude $\|\mathbf{u}\|/u'_0$ (left column) and normalized vorticity magnitude $\|\boldsymbol{\omega}\|L/u'_0$ (right column) on the xy plane at $z = L/2$ at time $t' = 0, 1.21, 6.08,$ and 12.16 (from top to bottom) with $N^3 = 128^3$. The solid red, green, and blue lines denote results of the PS, LBE, and DUGKS, respectively.

FIG. 2. Contours of normalized velocity magnitude $\|\mathbf{u}\|/u'_0$ (left column) and normalized vorticity magnitude $\|\boldsymbol{\omega}\|L/u'_0$ (right column) on the xy plane at $z = L/2$ at time $t' = 0, 1.21, 6.08,$ and 12.16 (from top to bottom) with $N^3 = 256^3$. The solid red, green, and blue lines denote results of the PS, LBE, and DUGKS, respectively.

kinetic energy contained only in the large eddies (i.e., at low wave numbers). This initial flow is unstable, and large

eddies will break up, transferring their energy successively to smaller and smaller eddies with high wave numbers until the


 FIG. 3. The energy spectra $E(k,t)$ with different mesh resolutions of (a) $N^3 = 128^3$ and (b) $N^3 = 256^3$ at $Re_\lambda = 26.06$.

eddy scale is sufficiently small, in which the eddy motions are stable and the viscosity is effective in dissipating the kinetic energy. After some time, a realistic DHIT will develop with some larger eddies supplying kinetic energy for smaller eddies, and the viscous action controls the size of the small eddies.

In the present work, the incompressible initial velocity field \mathbf{u}_0 ($\nabla \cdot \mathbf{u}_0 = 0$) is specified by a Gaussian field with a prescribed kinetic energy spectrum [17]:

$$E_0(k) := E(k, t = 0) = Ak^4 e^{-0.14k^2}, \quad k \in [k_{\min}, k_{\max}], \quad (25)$$

where k is the wave number, and the magnitude A and the range of the initial energy spectrum $[k_{\min}, k_{\max}]$ determine the total initial kinetic energy K_0 in the simulation. The kinetic energy

K , enstrophy, and dissipation rate ϵ are given, respectively, by

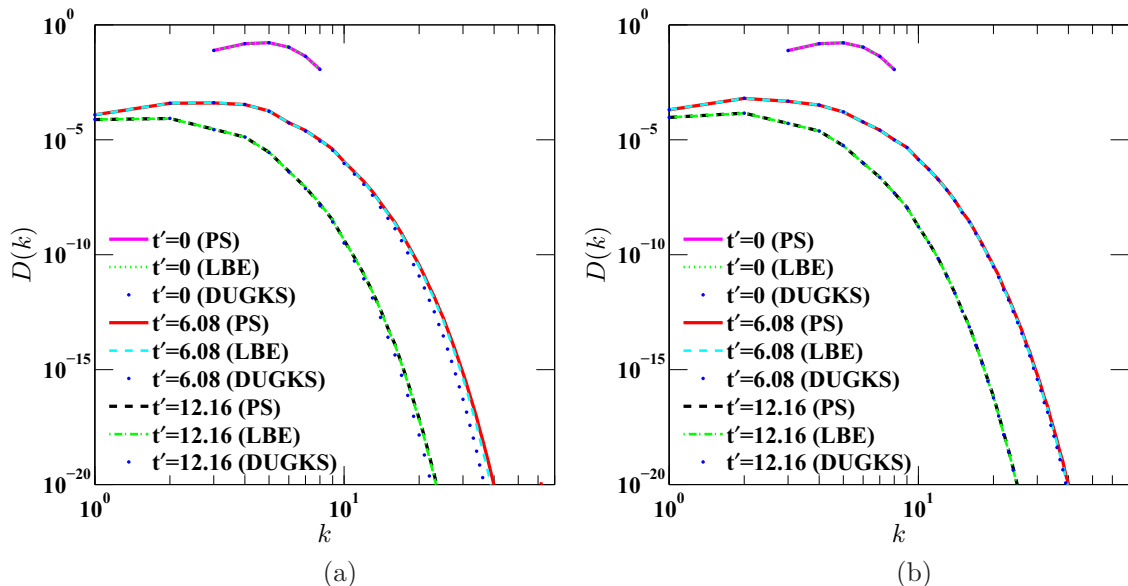
$$\begin{aligned} K(t) &= \int E(k,t) dk, & \Omega(t) &= \int k^2 E(k,t) dk, \\ \epsilon(t) &= 2\nu\Omega(t), \end{aligned} \quad (26)$$

where ν is the kinematic viscosity, and

$$E(\mathbf{k}, t) = \frac{1}{2} \hat{\mathbf{u}}(\mathbf{k}, t) \hat{\mathbf{u}}^*(\mathbf{k}, t), \quad (27)$$

where $\hat{\mathbf{u}}$ and $\hat{\mathbf{u}}^*$ are the velocity and its complex conjugate in the spectral space. The DHIT is typically characterized by the Taylor microscale Reynolds number,

$$Re_\lambda = \frac{u'\lambda}{\nu}, \quad (28)$$


 FIG. 4. The dissipation rate spectra $D(k,t)$ with different mesh resolutions of (a) $N^3 = 128^3$ and (b) $N^3 = 256^3$ at $Re_\lambda = 26.06$.

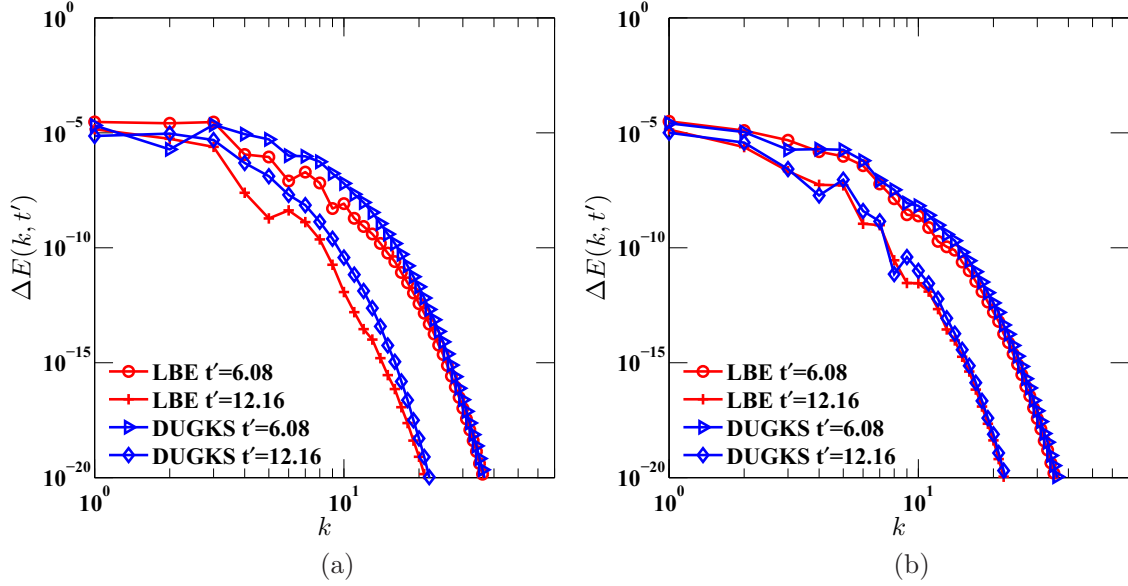


FIG. 5. The energy spectra difference $\Delta E(k, t')$ with different mesh resolutions of (a) $N^3 = 128^3$ and (b) $N^3 = 256^3$ at $Re_\lambda = 26.06$.

where u' is the root-mean-squared (rms) value of the turbulent fluctuating velocity \mathbf{u} in a given spatial direction and is defined by

$$u' = \frac{1}{\sqrt{3}} \sqrt{\langle \mathbf{u} \cdot \mathbf{u} \rangle}, \quad (29)$$

where $\langle \cdot \rangle$ designates the volume average, and λ is the transverse Taylor microscale length,

$$\lambda = \sqrt{\frac{15\nu}{\epsilon}} u'. \quad (30)$$

The other statistical quantities of interest are as follows:

$$\eta = \sqrt[4]{\nu^3/\epsilon}, \quad (31a)$$

$$D(k, t) = 2\nu k^2 E(k, t), \quad (31b)$$

$$S(t) = \frac{\langle (\partial_x u)^3 \rangle + \langle (\partial_y v)^3 \rangle + \langle (\partial_z w)^3 \rangle}{3[\langle (\partial_x u)^2 \rangle^{3/2} + \langle (\partial_y v)^2 \rangle^{3/2} + \langle (\partial_z w)^2 \rangle^{3/2}]}, \quad (31c)$$

$$F(t) = \frac{\langle (\partial_x u)^4 \rangle + \langle (\partial_y v)^4 \rangle + \langle (\partial_z w)^4 \rangle}{3[\langle (\partial_x u)^2 \rangle^2 + \langle (\partial_y v)^2 \rangle^2 + \langle (\partial_z w)^2 \rangle^2]}, \quad (31d)$$

where η is the Kolmogorov length and $D(k, t)$ is the energy dissipation rate spectrum; $S(t)$ and $F(t)$ are the velocity-derivative skewness and flatness averaged over three directions, respectively.

B. Kida vortex flow

The Kida vortex flow is another decaying turbulent flow that has been well studied using various LBE methods [20–22,48]. The flow evolves from a simple deterministic and symmetric

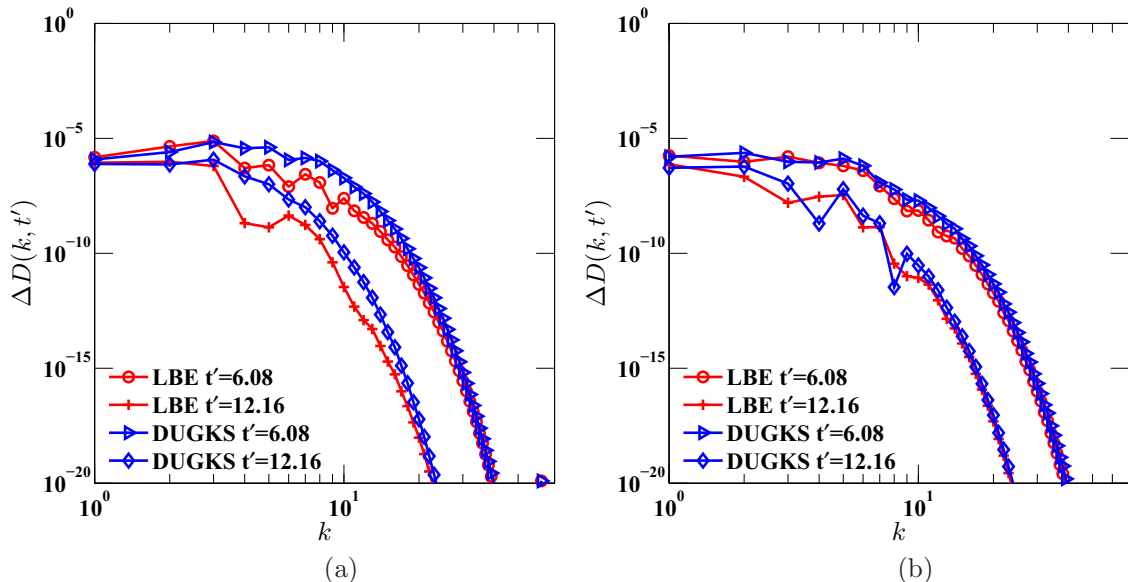


FIG. 6. The dissipation rate spectra difference $\Delta D(k, t)$ with different mesh resolutions of (a) $N^3 = 128^3$ and (b) $N^3 = 256^3$ at $Re_\lambda = 26.06$.

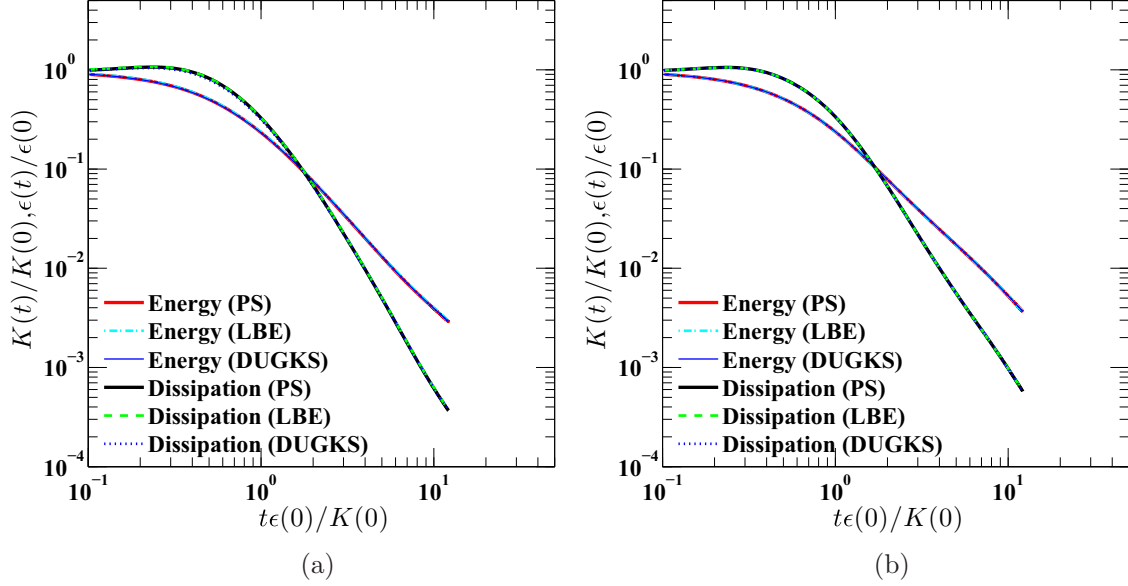


FIG. 7. Evolutions of the normalized total kinetic energy $K(t)/K_0$ and the normalized dissipation rate $\epsilon(t)/\epsilon_0$ with different mesh resolutions of (a) $N^3 = 128^3$ and (b) $N^3 = 256^3$ at $\text{Re}_\lambda = 26.06$.

initial condition to a state that resembles a fully developed turbulent flow. The initial conditions for the flow field are given by

$$u(x, y, z) = U_0 \sin x (\cos 3y \cos z - \cos y \cos 3z), \quad (32a)$$

$$v(x, y, z) = U_0 \sin y (\cos 3z \cos x - \cos z \cos 3x), \quad (32b)$$

$$w(x, y, z) = U_0 \sin z (\cos 3x \cos y - \cos x \cos 3y), \quad (32c)$$

where $x, y, z \in [0, 2\pi]$, U_0 is the initial velocity, and the periodic boundary conditions are imposed in all directions.

In addition to one-point statistics, we will also compare some two-point statistics for the Kida vortex flow, including the longitudinal correlation function [20,21]

$$\rho_{11}(r) = \frac{\langle u(x, y, z)u(x+r, y, z) \rangle}{\langle u(x, y, z)u(x, y, z) \rangle}, \quad (33)$$

transverse correlation functions

$$\rho_{22}(r) = \frac{\langle v(x, y, z)v(x+r, y, z) \rangle}{\langle v(x, y, z)v(x, y, z) \rangle}, \quad (34a)$$

$$\rho_{33}(r) = \frac{\langle w(x, y, z)w(x+r, y, z) \rangle}{\langle w(x, y, z)w(x, y, z) \rangle}, \quad (34b)$$

and the pressure-velocity correlation functions [49]

$$PU(r) = \langle |p(x, y, z)u(x, y, z) - p(x+r, y, z)u(x+r, y, z)| \rangle, \quad (35a)$$

$$PV(r) = \langle |p(x, y, z)v(x, y, z) - p(x+r, y, z)v(x+r, y, z)| \rangle, \quad (35b)$$

$$PW(r) = \langle |p(x, y, z)w(x, y, z) - p(x+r, y, z)w(x+r, y, z)| \rangle. \quad (35c)$$

IV. NUMERICAL RESULTS

A. Decaying homogeneous isotropic turbulence

1. Initial conditions

We perform the simulations of DHIT in a periodic box with the domain size L^3 using the LBE, DUGKS, and PS methods. The focus is on the comparison of LBE and DUGKS results with those from the PS method, which is used as a benchmark due to its superior spatial accuracy. The PS method is the same as in Ref. [17]. The units of LBE and DUGKS are converted back to the spectral units to allow for a direct comparison. The conversion requires a velocity scale V_s that is the ratio of the fluid velocity magnitude in LBE or DUGKS units to the velocity magnitude in spectral units.

In the PS simulation, the domain size is set to be $L^3 = (2\pi)^3$; for the initial energy spectrum $E_0(k)$ given by Eq. (25), we set $A = 1.7414 \times 10^{-2}$, $k_{\min} = 3$, and $k_{\max} = 8$ such that the initial kinetic energy is $K_0 = 0.9241$ and the rms velocity is $u'_0 = 0.7849$.

In the LBE and DUGKS simulations, we set the domain size $L^3 = N^3$, where N is the number of the cells or lattices in each spatial direction. In addition, we must ensure that the local Mach number (Ma) is small enough so that the flow is nearly incompressible, which can be met by choosing a suitable V_s . In the simulations, we chose a velocity scale $V_s = 0.0408$ that leads to the initial kinetic energy $K_0 = 1.5383 \times 10^{-3}$, the corresponding initial rms velocity $u'_0 = 0.0320$, and the

TABLE II. The maximum errors of $K(t)/K_0$ and $\epsilon(t)/\epsilon_0$ relative to PS results.

Case	LBE128	LBE256	DUGKS128	DUGKS256
$R_m(K)$	0.42%	0.34%	0.84%	0.49%
$R_m(\epsilon)$	0.83%	0.31%	3.90%	0.49%

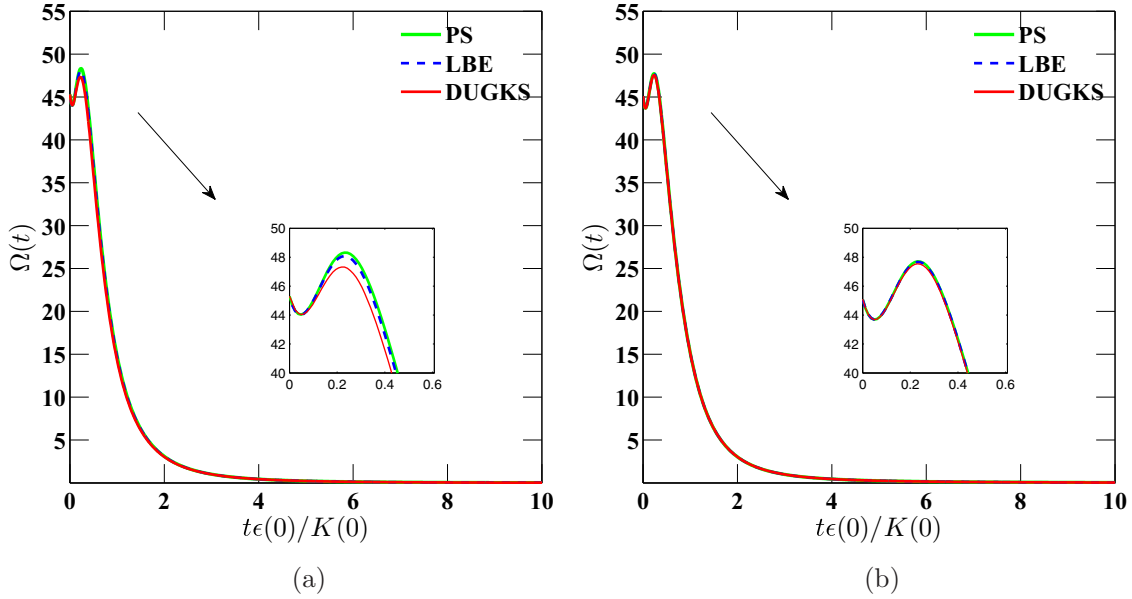


FIG. 8. Evolutions of the enstrophy Ω with different mesh resolutions of (a) $N^3 = 128^3$ and (b) $N^3 = 256^3$ at $Re_\lambda = 26.06$.

maximum velocity magnitude $\|\mathbf{u}_0\|_{\max} = 0.1660$ so that the maximum Mach number $Ma = \|\mathbf{u}_0\|_{\max}/c_s = 0.2875$, here $c_s = \sqrt{RT}$, $RT = 1/3$. The initial velocity field and parameters used in the LBE and DUGKS simulations are identical except the time step size Δt . In the LBE method, the time step size $\Delta t = \Delta x = 1$ in LBE units, while in DUGKS it is solely determined by the CFL condition, i.e., $\Delta t = \gamma \Delta x_{\min}/\sqrt{2}c$, where γ is the CFL number, Δx_{\min} is the minimum grid spacing, and $\sqrt{2}c$ is the maximum discrete particle speed in D3Q19. In the DUGKS simulations, we set $\gamma = 0.7071$ such that the time step $\Delta t = 0.5$ for convenient comparison. Moreover, for the MRT-LBE, the specific parameters are

set to be $\omega_\varepsilon = \omega_{xx} = 0$, $\omega_{ej} = -475/63$, $s_2 = s_{10} = 1.4$, $s_9 = s_{13} = \Delta t/(3\nu + 0.5\Delta t)$, $s_1 = 1.19$, $s_4 = 1.2$, and $s_{16} = 1.98$ [13].

Table I summarizes the parameters used in the simulations with these three methods. Two mesh resolutions are considered in the simulations. To fix the initial Taylor microscale Reynolds number $Re_\lambda = 26.06$, in the PS simulation we set the kinematic viscosity $\nu = 1.4933 \times 10^{-2}$ for both resolutions, while in the LBE and DUGKS simulations we set the viscosity $\nu = 1.2395 \times 10^{-2}$ and 2.4790×10^{-2} for the mesh resolutions of 128^3 and 256^3 , respectively. It should be noted that the flow is overresolved in the PS simulations as the minimum spatial

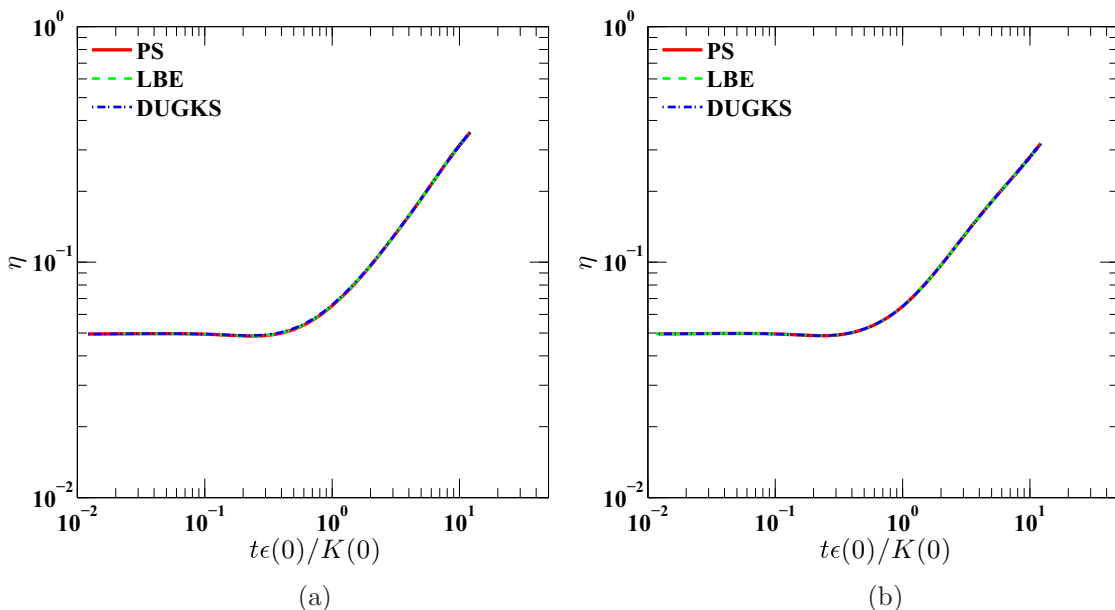
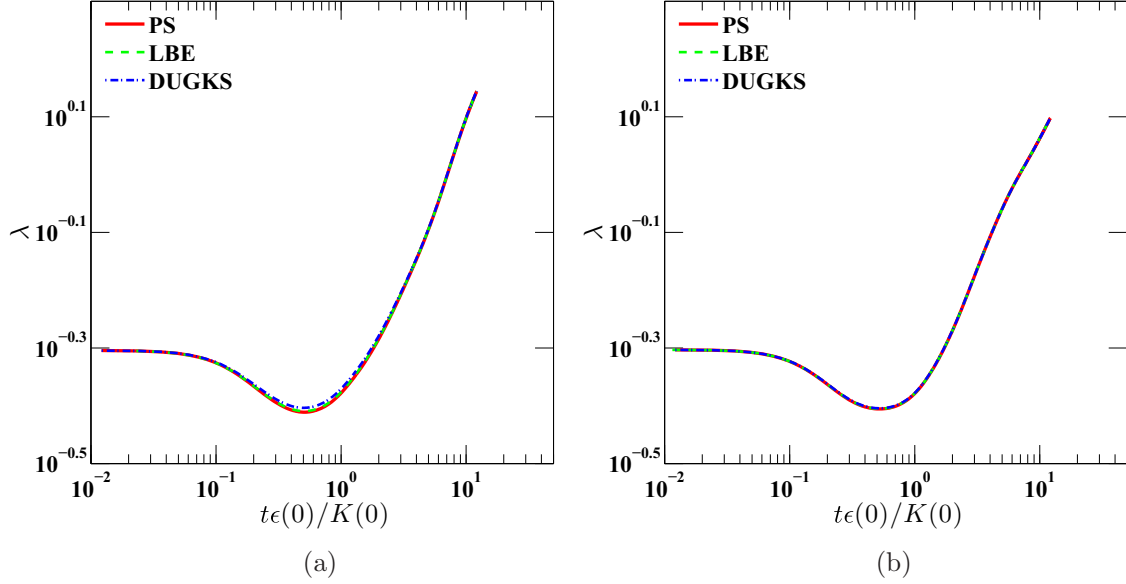


FIG. 9. Evolutions of the Kolmogorov length η with different mesh resolutions of (a) $N^3 = 128^3$ and (b) $N^3 = 256^3$ at $Re_\lambda = 26.06$.


 FIG. 10. Evolutions of the Taylor microscale length λ with different mesh resolutions of (a) $N^3 = 128^3$ and (b) $N^3 = 256^3$ at $\text{Re}_\lambda = 26.06$.

resolution parameter $k_{\max}\eta$ is larger than 2.07 at 128^3 and 4.15 at 256^3 , respectively, where k_{\max} is the maximum resolved wave number [50]. This implies that the results from the PS simulations at the two grid resolutions would be identical. The nondimensional time step size, normalized by the turbulence eddy turnover time $t_0 = K_0/\epsilon_0$, is $\Delta t' = \Delta t\epsilon_0/K_0$.

With the initial velocity field \mathbf{u}_0 , the initial pressure p_0 is obtained by solving the Poisson equation in the spectral space for the PS method. As for the LBE and DUGKS methods, besides the pressure p_0 , herein related to the density fluctuation by an equation of state, a consistent initial distribution function including the nonequilibrium part should be specified, which is achieved by using the iterative procedure described in [51].

2. Instantaneous velocity and vorticity fields

We compare the instantaneous velocity and vorticity magnitude obtained by LBE and DUGKS methods with those from PS simulation on the xy plane at $z = L/2$. The vorticity fields for all three methods are first computed in the spectral space, $\tilde{\omega} = i\mathbf{k} \times \tilde{\mathbf{u}}$, and then $\tilde{\omega}$ is transferred back to the physical space using inverse fast Fourier translation (FFT).

Figure 1 shows the contours of normalized velocity magnitude $\|\mathbf{u}\|/u'_0$ and vorticity magnitude $\|\omega\|L/u'_0$ at different nondimensional times $t' = 0, 1.21, 6.08, \text{ and } 12.16$ on a mesh of $N^3 = 128^3$. As shown in Figs. 1(a) and 1(b), these three methods have the identical initial fields with many large eddies; then small scale eddies are produced by vortex stretching as shown in Figs. 1(c) and 1(d); in the end, as shown in Figs. 1(g) and 1(h), the small scale eddies are dissipated by viscous

actions. As shown in these figures, although the fields predicted by the LBE and DUGKS methods are similar to each other, and very close to those from the PS simulation in terms of vortex shapes and locations, the discrepancy between both kinetic methods and the PS method is still visible and increases over time.

We also conduct the simulations on a finer mesh of 256^3 at $\text{Re}_\lambda = 26.06$. As shown in Fig. 2, again the velocity magnitude (left column) and vorticity magnitude (right column) obtained from the LBE and DUGKS methods are in good agreement with those from the PS method. It can be seen that both kinetic methods with their fine resolution give much better predictions than those with a coarse resolution.

3. Statistical quantities

In this subsection, we compare some key statistical quantities, including both the low- and high-order statistical quantities, obtained by the LBE and DUGKS methods with those from the PS method. The simulations of these three methods are performed on both $N^3 = 128^3$ and 256^3 mesh resolutions.

We first compare the energy spectra $[E(k)]$ and dissipation spectra $[D(k)]$ at $t' = 0, 6.08, \text{ and } 12.16$. As shown in Figs. 3(a) and 4(a), the results computed by the LBE and DUGKS agree well with those from the PS counterparts. It should be noted that although there are a few deviations in the high-wave-number region for the results of DUGKS on the mesh of 128^3 , the values of both spectra have decreased to the 10^{-10} magnitude of the maximum initial value, which will not cause significant deviations in the integral quantities, such as the normalized kinetic energy K/K_0 and dissipation rate ϵ/ϵ_0 shown in Fig. 7(a). This discrepancy may be caused by the numerical dissipation, which is proportional to the mesh size. Therefore, we can refine the mesh resolution to reduce the numerical dissipation. As expected, as shown in Figs. 3(b) and 4(b), with a mesh resolution of 256^3 , the results of DUGKS

 TABLE III. The maximum errors of λ and η relative to PS results.

Case	LBE128	LBE256	DUGKS128	DUGKS256
$R_m(\lambda)$	0.21%	0.08%	1.00%	0.12%
$R_m(\eta)$	0.44%	0.12%	1.84%	0.27%

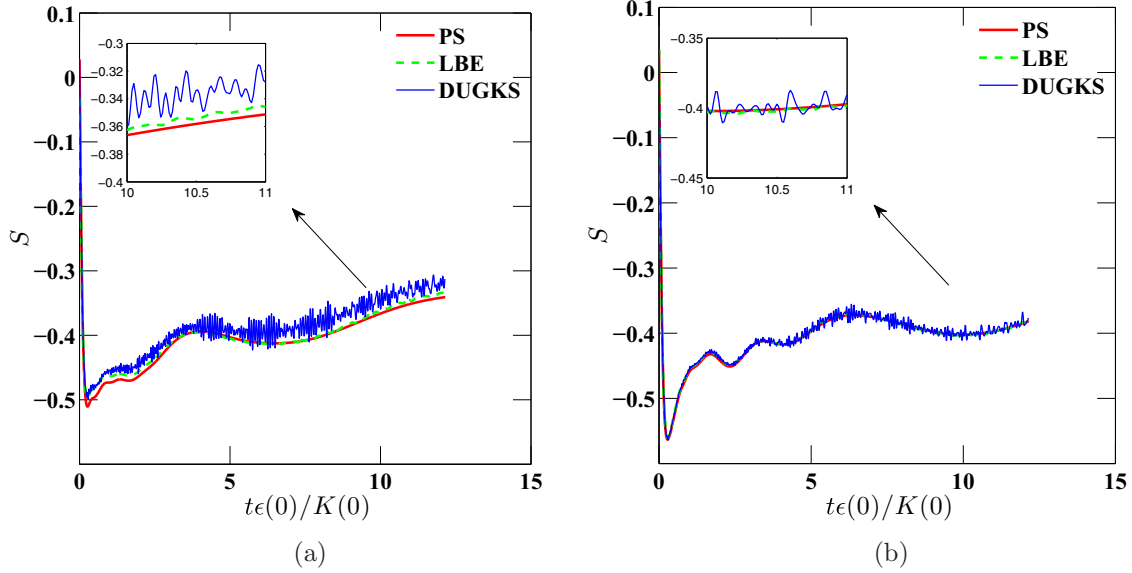


FIG. 11. Evolutions of velocity-derivative skewness S with different mesh resolutions of (a) $N^3 = 128^3$ and (b) $N^3 = 256^3$ at $Re_\lambda = 26.06$.

show no visible difference with those from the LBE and PS simulations. We also compute the difference of the spectra between both kinetic methods and the PS method, which is defined by

$$\Delta S(k, t') = \|S(k, t') - S_p(k, t')\|, \quad (36)$$

where S denotes the results of energy spectra or dissipation rate spectra, and S_p represents the results from the PS simulations. Figures 5 and 6, respectively, show the differences of energy spectra $\Delta E(k, t')$ and dissipation rate spectra $\Delta D(k, t')$ on both meshes. We observe that with a mesh of 128^3 , the results obtained by LBE are slightly better than those from the DUGKS when compared with the PS results, but there is no visible difference when both methods use a fine mesh of 256^3 . These results indicate that the dissipation of the DUGKS is

slightly larger than that of the LBE method, although both the LBE and DUGKS methods have low numerical dissipation.

Secondly, we compare the evolutions of normalized kinetic energy $K(t)/K_0$ and dissipation rate $\epsilon(t)/\epsilon_0$. As shown in Fig. 7, both $K(t)/K_0$ and $\epsilon(t)/\epsilon_0$ calculated by the LBE and DUGKS methods are in excellent agreement with those from PS simulation on both meshes. Quantitatively, we compare the maximum errors of $K(t)$ and $\epsilon(t)$ relative to the PS results, which is defined by

$$R_m(s) = \left\| \frac{s - s_p}{s_p} \right\|_{\max}, \quad (37)$$

where $s = K(t)$ or $\epsilon(t)$, and s_p is the corresponding quantity from the PS method. Here we assume that the flow is regarded as adequately resolved when the relative error of the dissipation

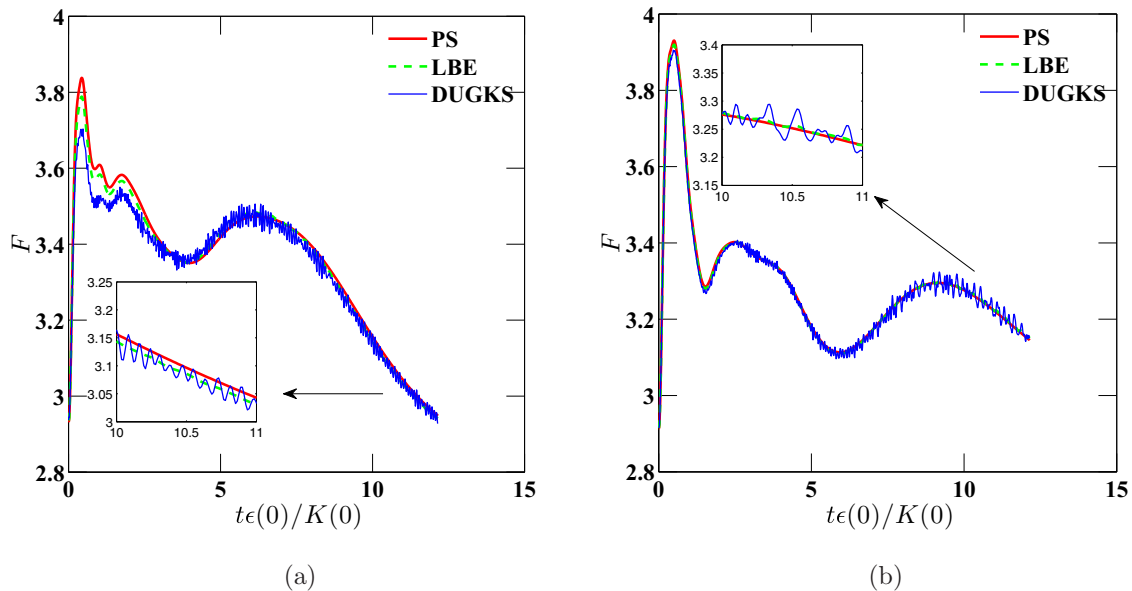


FIG. 12. Evolutions of velocity-derivative flatness F with different mesh resolutions of (a) $N^3 = 128^3$ and (b) $N^3 = 256^3$ at $Re_\lambda = 26.06$.

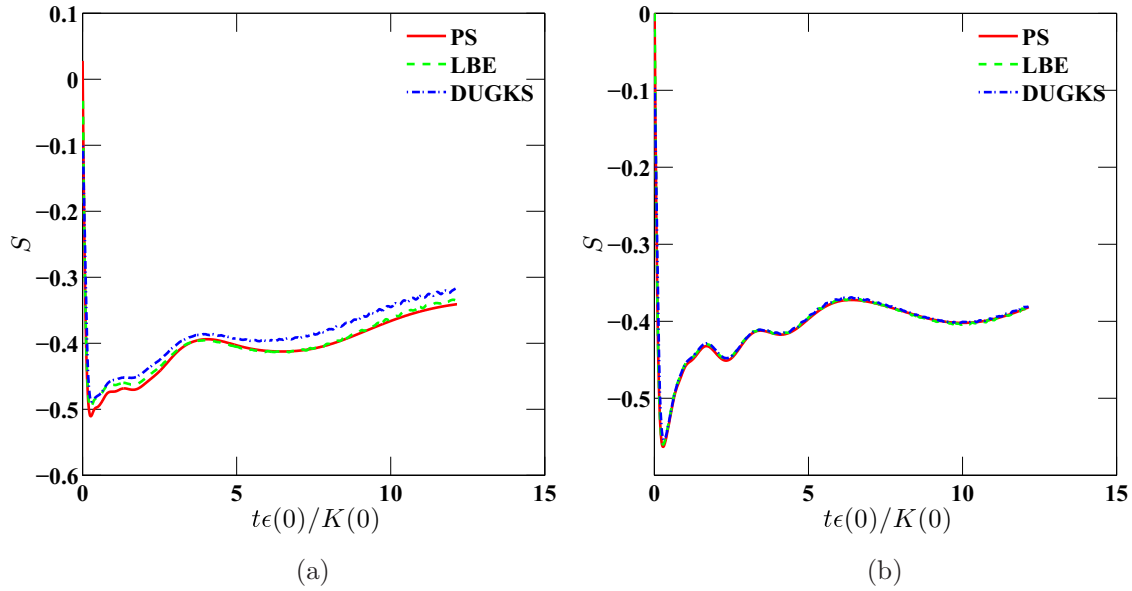


FIG. 13. Evolutions of smoothed velocity-derivative skewness S with different mesh resolutions of (a) $N^3 = 128^3$ and (b) $N^3 = 256^3$ at $Re_\lambda = 26.06$.

rate $R(\epsilon)$ is less than 4%. As shown in Table II, the maximum relative errors are less than 1% except that of $\epsilon(t)$ from the DUGKS with $N^3 = 128^3$, which reaches 3.9% around the peak value, and it decreases to 0.49% in the 256^3 simulation. Although these discrepancy can be seen more clearly from the evolution of the enstrophy shown in Fig. 8(a), the maximum relative difference is less than 4%, which means that the given flow is adequately resolved by the DUGKS with the minimum spatial resolution parameter $k_{\max}\eta = 3.12$. Moreover, these difference can be reduced by using the finer mesh with the minimum $k_{\max}\eta = 6.24$ as shown in Fig. 8(b), which indicates

that the DUGKS is more dissipative than the LBE method. We also observe that the normalized energy dissipation rate attains a peak value at $t' = 0.23$ due to the energy cascade, before decreasing with increasing time due to the viscous dissipation.

Thirdly, we compare the evolutions of the Kolmogorov length λ and the Taylor microscale length η . The Kolmogorov length is the smallest scale in turbulence flow, at which the viscous effect dominates and the turbulence kinetic energy is converted irreversibly into heat. The Taylor microscale is the intermediate scale between the largest and the smallest scales at which fluid viscosity significantly affects the dynamics

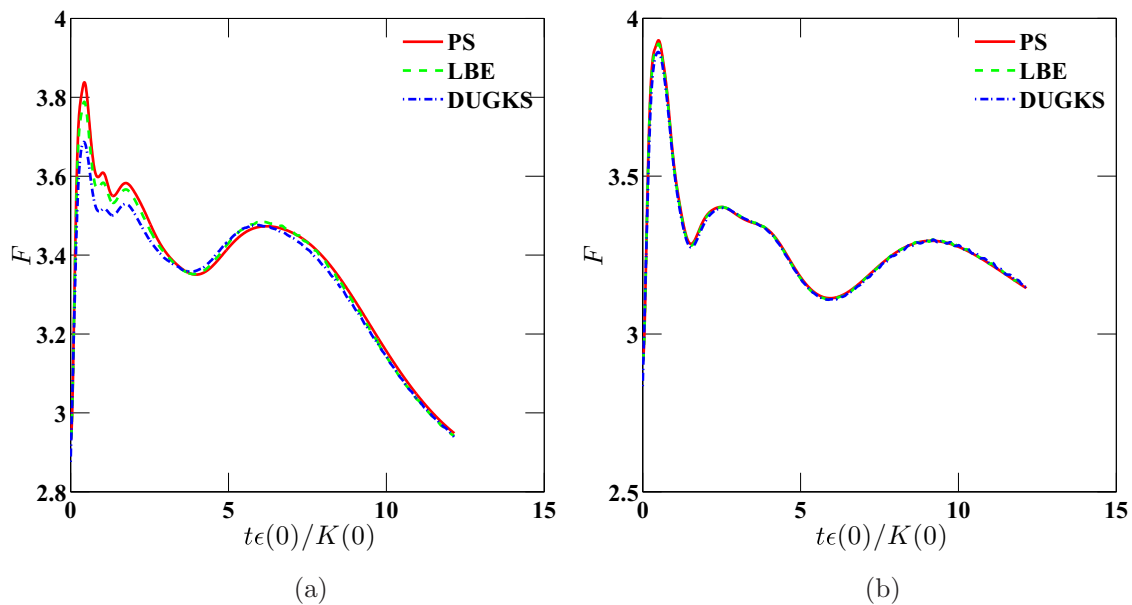


FIG. 14. Evolutions of smoothed velocity-derivative flatness F with different mesh resolutions of (a) $N^3 = 128^3$ and (b) $N^3 = 256^3$ at $Re_\lambda = 26.06$.

TABLE IV. The maximum errors of S and F relative to PS results.

Case	LBE128	LBE256	DUGKS128	DUGKS256
$R_m(S)$	3.35%	4.52%	11.97%	4.98%
$R_m(F)$	1.30%	0.35%	3.97%	1.11%

of turbulent eddies in the flow. Figures 9 and 10 show the evolutions of the Kolmogorov length scale and the Taylor microscale length. It is found that results of both scales from the DUGKS and the LBE methods agree well with those from the PS method. We also note that there are slight differences around the minimum of λ obtained by the DUGKS with the mesh resolution of 128^3 , but as shown in Table III, the maximum relative errors of λ and η are all less than 2%, and they reduce to 0.27% as the resolution increases to 256^3 .

The time evolutions of the averaged velocity-derivative skewness and flatness predicted by these three methods are shown in Figs. 11 and 12, respectively. It can be seen that the results of the LBE with a mesh of 128^3 are in good agreement with the PS solutions, while those of the DUGKS show some high-frequency oscillations, although the tendency agrees reasonably well with the results from the PS simulation. The oscillations can be attributed to the acoustic waves in the system. The remarkable discrepancy between the LBE and DUGKS results may be due to the following reasons: First, in the MRT-LBE model, the bulk viscosity can be adjusted by tuning the relaxation time s_1 to absorb the acoustic waves, whereas the BGK-based DUGKS does not have such a dissipation mechanism due to the single relaxation time in the BGK equation. Actually, the results of the MRT-LBE with small bulk viscosity also have high-frequency oscillations shown in Ref. [17], where the bulk viscosity $\zeta = 0.0273$ compared to $\zeta = 0.1134$ in the present simulation. Second, since the velocity-derivative skewness and flatness are the third- and four-order moments of $\nabla \mathbf{u}$, respectively, it is a significant challenge for a second-order method to

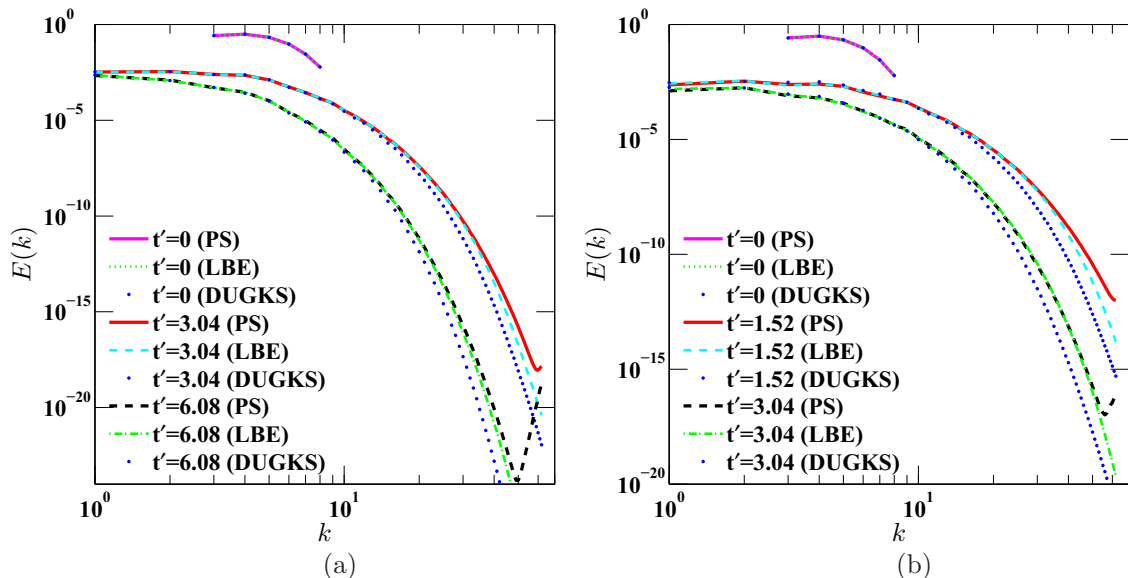
compute such high-order quantities that are governed by small scales. As demonstrated, both the LBE and DUGKS methods have small numerical dissipation so that both methods can accurately compute the low-order statistic quantities that are governed by large scales. However, the numerical dissipation of DUGKS is slightly larger than the LBE method, and yet the absent acoustic-wave dissipation mechanism enlarges the discrepancy as the velocity field decays and consequently results in errors in high-order quantities. The high-order errors, however, seem to have little impact on the kinetic energy and dissipation rate.

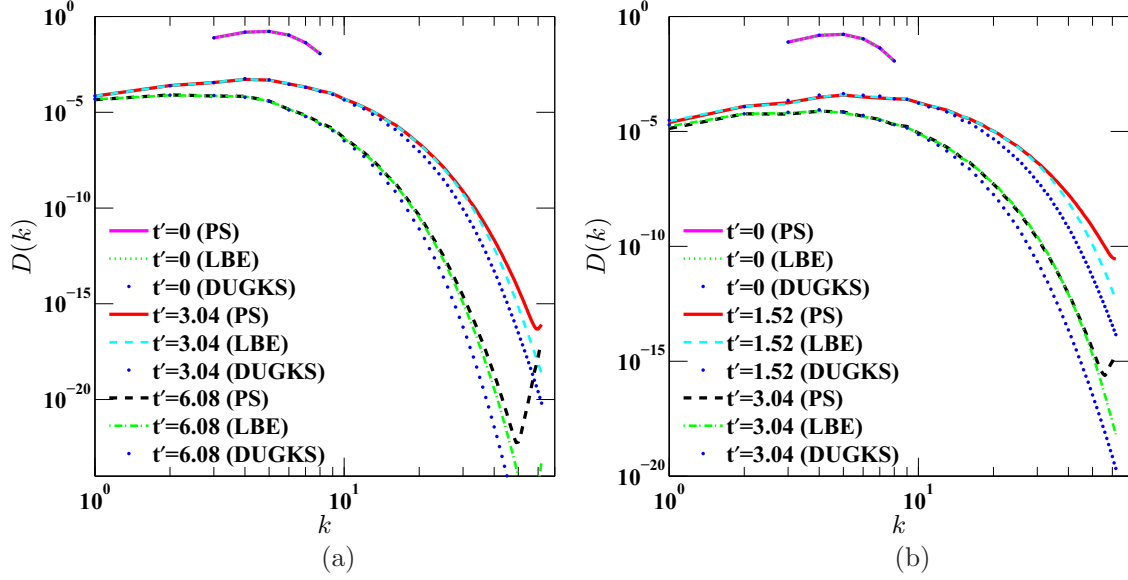
As previously noted, increasing the mesh resolution can reduce the numerical dissipation, thus better results should be obtained in 256^3 simulations. As expected, as shown in Figs. 11(b) and 12(b), the results of DUGKS with $N^3 = 256^3$ are better than those with the coarse mesh, and the magnitudes of the oscillations are also reduced.

For convenient comparison, the results of the DUGKS can be filtered out by simply smoothing through averaging (using the smooth function in MATLAB), as suggested in Ref. [17]. The smoothed skewness and flatness results are shown in Figs. 13 and 14, respectively. It is found that both LBE and DUGKS results indeed agree well with the PS results. Quantitatively, as given in Table IV, the maximum relative error of S predicted by the DUGKS with a mesh of 128^3 is 11.97%, while for the LBE this value is 3.35%. As the resolution increases to 256^3 , the maximum relative error of S computed by the DUGKS reduces to 4.98%.

4. Effects of the Reynolds number

In the above subsections, we have made some detailed comparisons between the LBE and DUGKS methods with the initial $\text{Re}_\lambda = 26.06$, at which the initial flow fields can be well-resolved by both methods. To further compare the performance of the LBE and DUGKS methods at higher Re_λ , we conduct the DNS of the DHIT at $\text{Re}_\lambda = 52.12$ and 104.24 with a fixed mesh of 128^3 . Accordingly, in the

FIG. 15. The energy spectra $E(k, t)$ at (a) $\text{Re}_\lambda = 52.12$ and (b) $\text{Re}_\lambda = 104.24$.

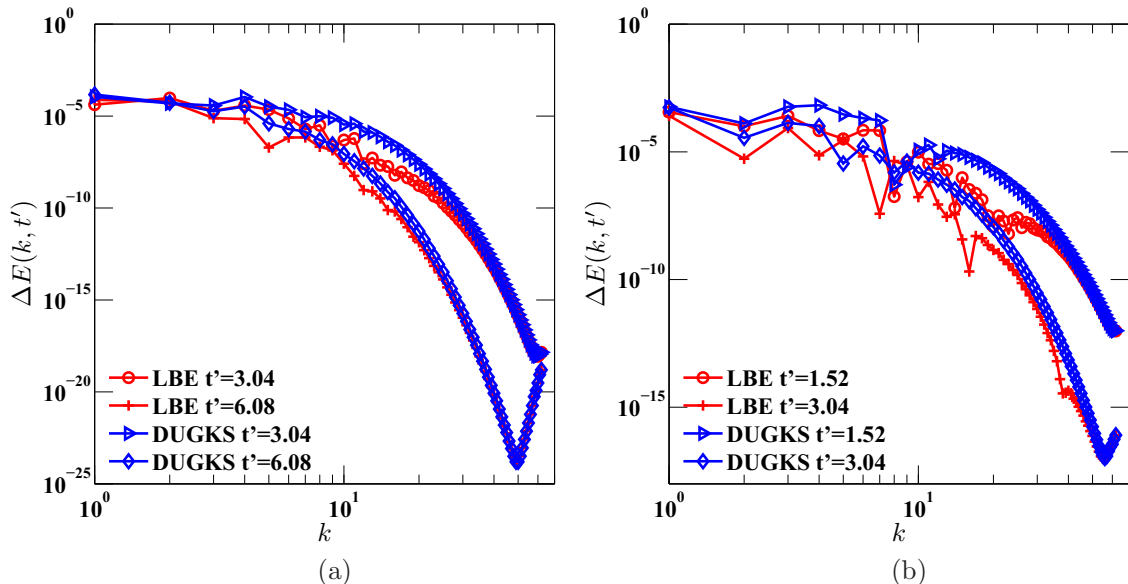

 FIG. 16. The dissipation rate spectra $D(k, t)$ at (a) $Re_\lambda = 52.12$ and (b) $Re_\lambda = 104.24$.

PS simulation, the minimum spatial resolution parameters $k_{\max}\eta$ are 1.33 for $Re_\lambda = 52.12$ and 0.83 for $Re_\lambda = 104.24$, suggesting that the PS method can adequately resolve the flow field at $Re_\lambda = 52.12$ [50]. In addition, values of the minimum $k_{\max}\eta$ for LBE and DUGKS with a mesh of 128^3 are 2 for $Re_\lambda = 52.12$ and 1.26 for $Re_\lambda = 104.24$, respectively, indicating that the flow at $Re_\lambda = 52.12$ can be adequately resolved by the LBE method [17]. However, it is not clear whether this resolution is sufficient for the DUGKS method at these Re_λ . Herein, we compare some key statistical quantities obtained by both kinetic approaches at these Re_λ with those from the PS simulations.

Figures 15 and 16 show the energy spectra $E(k, t)$ and the dissipation rate spectra $D(k, t)$ at different times. It is observed that $E(k, t)$ and $D(k, t)$ obtained by the LBE method are still

in good agreement with those from the PS method, while the results from the DUGKS clearly deviate from the PS results in the high-wave-number region, and the discrepancies increase with Re_λ . The differences of the spectra between both kinetic methods and the PS method, as defined by Eq. (36), are shown in Figs. 17 and 18. It can be clearly seen that the LBE method yields better predictions than the DUGKS.

We also compare the evolutions of the normalized kinetic energy and the dissipation rate. As shown in Fig. 19, $K(t)/K_0$ obtained by the LBE and DUGKS methods are in good agreement with the PS results. However, the differences are visible around the peak values of $\epsilon(t)/\epsilon_0$ computed by both methods, and it can be clearly seen that the LBE method gives a better prediction than the DUGKS. For example, at $Re_\lambda = 52.12$, for the LBE the maximum relative error of ϵ is


 FIG. 17. The energy spectra difference $\Delta E(k, t')$ at (a) $Re_\lambda = 52.12$ and (b) $Re_\lambda = 104.24$.

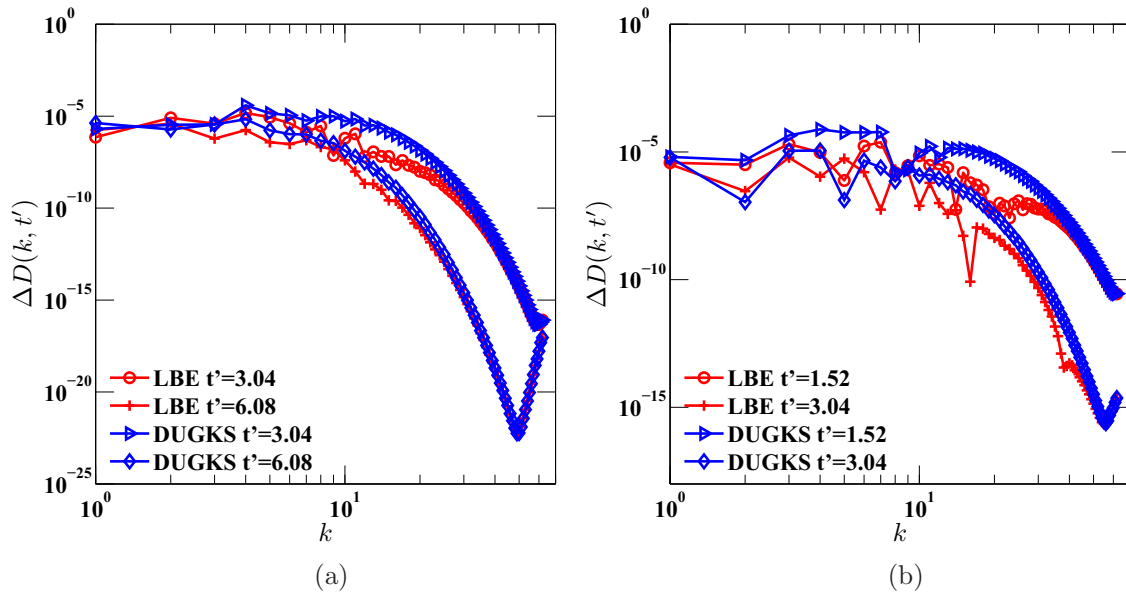


FIG. 18. The dissipation rate spectra difference $\Delta D(k, t)$ at (a) $Re_\lambda = 52.12$ and (b) $Re_\lambda = 104.24$.

1.85%, while for the DUGKS it is 11.6%. This indicates that with the minimum $k_{max}\eta = 2.0$, the given flow field is well resolved by the LBE method, but not the DUGKS. Similar phenomena can also be observed from the evolution of the enstrophy shown in Fig. 20 for the given Reynolds numbers, especially the discrepancy around the peak values, as shown in the insets. Similar results are also obtained from the evolutions of the Kolmogorov length η and the Taylor microscale length λ , which are shown in Figs. 21 and 22, respectively. We observe that the maximum deviation appears around the minima of η or λ , where the adequate spatial resolution in the DUGKS and LBE is most likely not met. It can be clearly found that the LBE is more accurate than the DUGKS in capturing both scales due to the lower numerical dissipation in the LBE.

Finally, in order to figure out the effects of the Reynolds number on the flow fields for the DUGKS, we also compare the vorticity fields predicted by both methods. Figures 23 and 24 show the snapshots of the vorticity at $Re_\lambda = 52.12$ and 104.24, respectively. It can be clearly seen that the DUGKS results deviate from the LBE results at later times, and the difference is larger for larger Re . It should be noted that although in DUGKS the pressure fluctuation will increase with the Reynolds number under the given mesh resolution, these fluctuations do not deteriorate the flow fields, which are still smooth at high Re_λ , as shown in Figs. 23 and 24.

Based on the above observations, we can conclude that the LBE gives more accurate results than the DUGKS at both Re_λ with underresolved meshes. Specifically, with the minimum

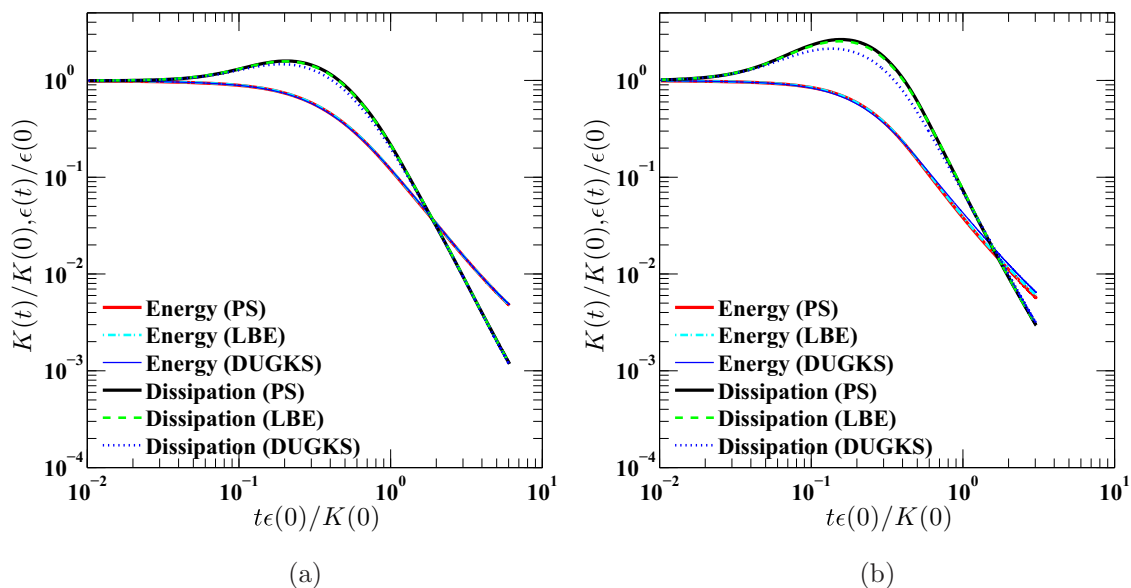


FIG. 19. Evolutions of the normalized total kinetic energy $K(t)/K_0$ and the normalized dissipation rate $\epsilon(t)/\epsilon_0$ at (a) $Re_\lambda = 52.12$ and (b) $Re_\lambda = 104.24$.

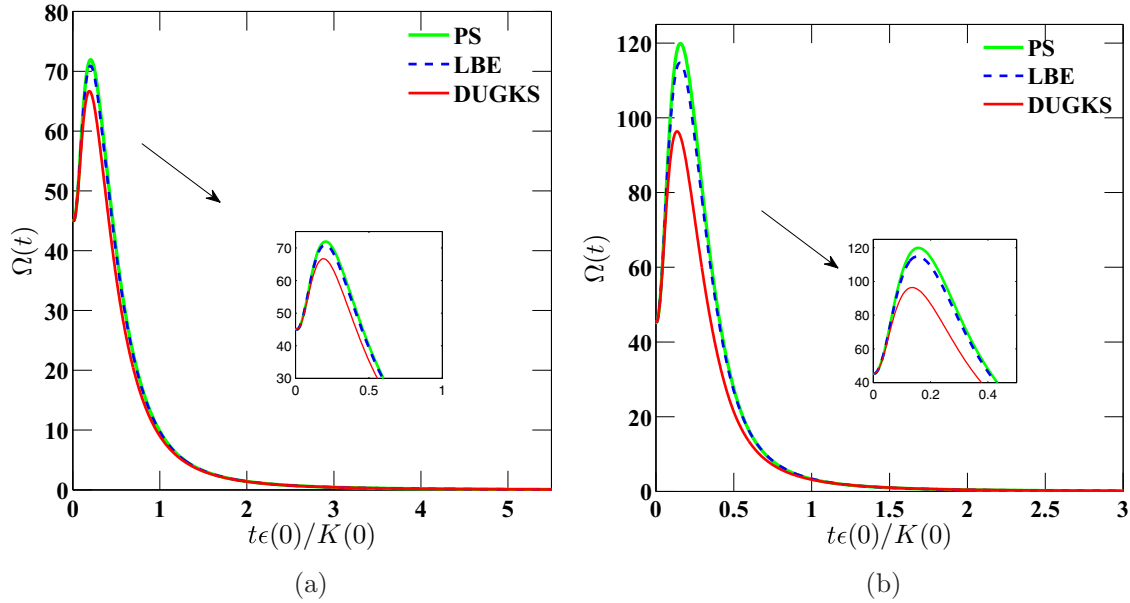


FIG. 20. Evolutions of the enstrophy Ω at (a) $Re_\lambda = 52.12$ and (b) $Re_\lambda = 104.24$.

spatial resolution parameter $2 < k_{max}\eta < 3$, the flow fields can be adequately resolved by the LBE method, but they are not adequately resolved by the DUGKS, particularly in the high-wave-number region, which represents the small-scale turbulent eddies. This means that the DUGKS has relatively larger numerical dissipation than the LBE.

It is interesting to figure out the reasoning behind the more dissipative nature of the DUGKS than the LBE. One of the major reasons is that as a finite volume scheme, additional numerical dissipation is introduced in the DUGKS in the initial data reconstruction. It should be noted that although the DUGKS is more dissipative than the LBE method, we argue that the coupled collision and transport mechanism in the flux reconstruction can ensure that the DUGKS still has relatively low numerical dissipation when compared with the

direct unwinding reconstruction of the original distribution function without considering the collision effects [43,44]. It should be noted that the CFL number γ in DUGKS we adopt is 0.7071, which is relatively large for such a kinetic scheme. Actually, since the physical model, rather than interpolation, is directly applied to reconstruct the flux across the cell interface, the dissipation will decrease with reducing CFL number or increasing the nonuniformities of the mesh according to the local accuracy requirement, which has been demonstrated in the previous work [45,52].

5. Computational efficiency and numerical stability

Finally, we compare the computational efficiency of the LBE and DUGKS methods on a fixed mesh of 128^3 . For each

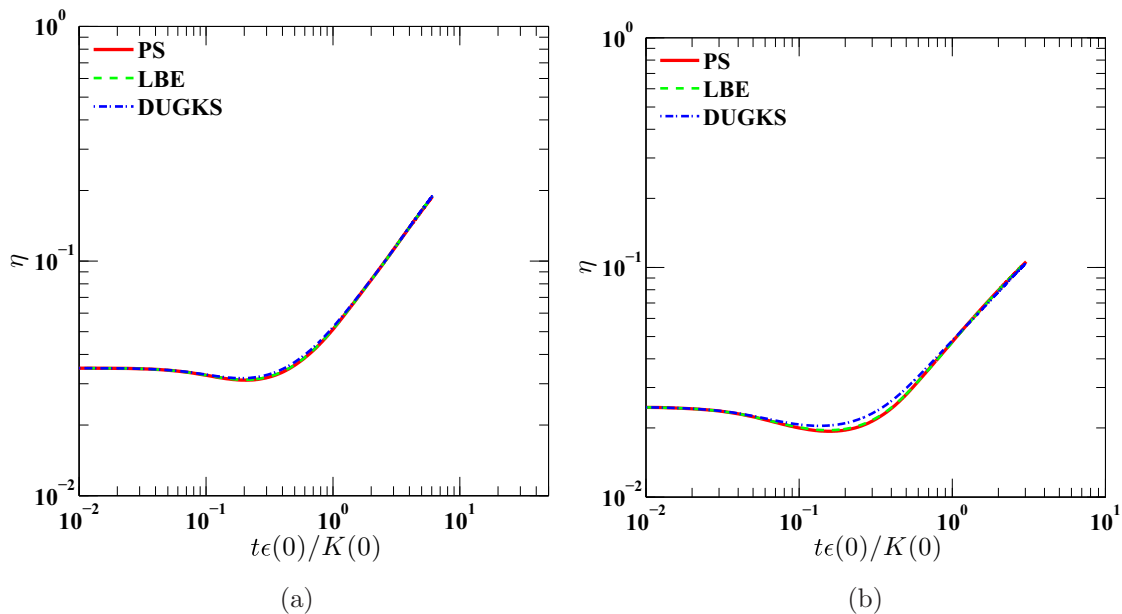


FIG. 21. Evolutions of the Kolmogorov length η at (a) $Re_\lambda = 52.12$ and (b) $Re_\lambda = 104.24$.

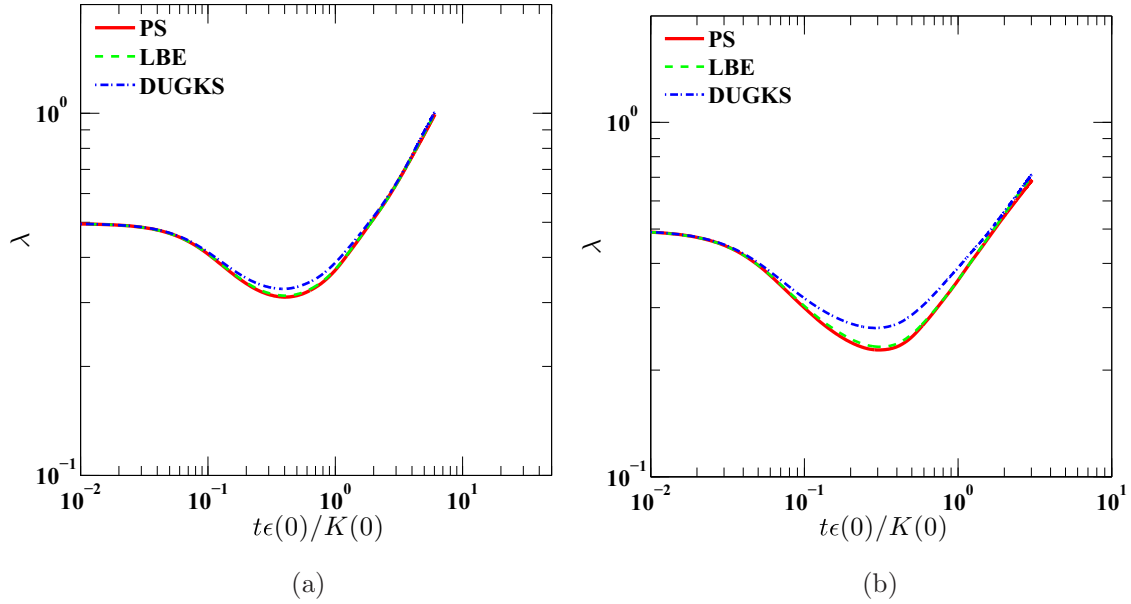


FIG. 22. Evolutions of the Taylor microscale length λ at (a) $\text{Re}_\lambda = 52.12$ and (b) $\text{Re}_\lambda = 104.24$.

iteration, the CPU time costs of the LBE and DUGKS are 0.666 and 0.911 s, respectively, where both codes run on 16 cores based on the message passing interface (MPI) using two-dimensional domain decomposition. Therefore, the LBE method is about 36.8% faster than the DUGKS per time step. But, due to the different time steps used in the two methods, in our simulations two DUGKS time steps are equivalent to one LBE time step.

In terms of the numerical stability, we compute the maximum stable Taylor microscale Reynolds number of both LBE and DUGKS codes on a mesh of 128^3 . In the simulations, we set the CFL number to be 0.9 in the DUGKS in order to make a fair comparison with the LBE in which the CFL number equals 1.0. Without considering the accuracy, the LBE code blows up when the Taylor microscale Reynolds number reaches $\text{Re}_\lambda = 26\,060$, while the DUGKS is still stable at such Re_λ . Therefore, the DUGKS is more stable than the LBE methods, which is consistent with the previous study [45].

B. Kida vortex flow

The above results indicate that the flow can be adequately resolved by the DUGKS with the minimum spatial resolution parameter $k_{\max}\eta$ larger than 3. To further validate this conclusion as well as the accuracy of the DUGKS for DNS of decaying turbulent, in this subsection the Kida vortex flow is simulated by the DUGKS and compared with the well-resolved LBE results.

1. Initial condition

The Reynolds number for the Kida vortex flow is defined by $\text{Re} = LU_0/\nu$, where L is the domain size and ν is the kinematic viscosity. The initial pressure field as well as a consistent initial distribution are obtained by an iterative procedure with the given initial velocity field [Eq. (32)] [51].

In the simulation, we set the domain size $L = N$, where N is the grid size in each direction. The velocity and time

presented in the results are normalized by U_0 and L/U_0 , respectively. It should be noted that the previous results have clearly demonstrated that the accuracy of the standard LBE method is comparable to the PS method, and the LBE can give the well-resolved result when the minimum spatial resolution parameter $k_{\max}\eta$ is larger than 2.0 [17], thus for the Kida vortex flow simulation, the LBE results are adopted as benchmark data to validate the accuracy of the DUGKS.

The simulation is performed for a relatively low Reynolds number $\text{Re} = 2000$, which is sufficient for comparison. We set the computational domain size $L^3 = 256^3$ with a mesh of $N^3 = 256^3$, and the corresponding minimum $k_{\max}\eta$ is 3.29, which guarantees that the results obtained by the LBE are adequately resolved. The velocity U_0 is set to be 0.05 such that the flow is nearly incompressible, and the CFL number is again set to be $\gamma = 0.7071$ so that the time step Δt in DUGKS is equal to 0.5.

2. Instantaneous vorticity fields

Figure 25 shows the normalized vorticity $\|\omega\|L/U_0$ on the xy plane of $z = L/2$ at different normalized times $t = 0, 0.9765, 1.9531, \text{ and } 2.9297$. As shown in Fig. 25(a), both the LBE and DUGKS methods have identical initial fields containing only large eddies. These large eddies are unstable, and they produce small eddies by vortex stretching as shown in Figs. 25(b) and 25(c). In the end, as shown in Fig. 25(d), the small eddies are dissipated by the viscous actions. In addition, it is found that although vorticity snapshots predicted by the LBE and DUGKS methods are very similar to each other in terms of the vortex shapes and locations at the initial stage, the discrepancy between the two methods is still visible and increases over time. All these results are similar to those of the DNS of DHIT.

3. Statistical quantities

We study first the one-point statistics of the Kida vortex flow. Figure 26(a) shows the evolution of the normalized

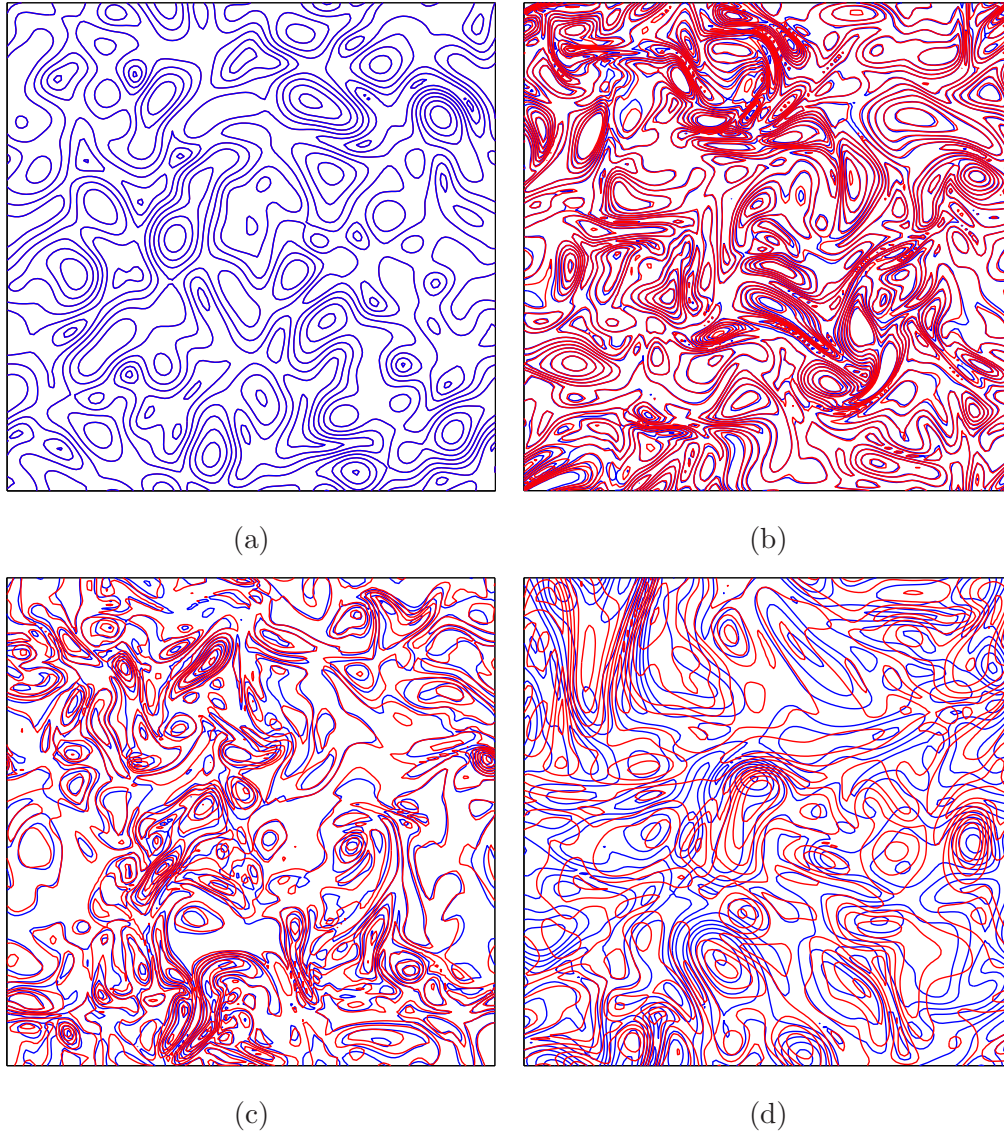


FIG. 23. Contours of normalized vorticity magnitude $\|\omega\|L/u'_0$ on the xy plane at $z = L/2$ at time (a) $t' = 0$, (b) $t' = 0.12$, (c) $t' = 0.6$, and (d) $t' = 3$ for $Re_\lambda = 52.12$. The solid red and blue lines denote results of the LBE and DUGKS, respectively.

kinetic energy K and dissipation rate ϵ obtained from the LBE and DUGKS methods. As shown, the results of K and ϵ calculated by the DUGKS agree well with the LBE results. In particular, the maximum relative error of dissipation rate compared with the LBE results is less than 4%, which shows that the flow is adequately resolved by DUGKS with the minimum spatial resolution parameter $k_{\max}\eta = 3.29$. Similar results are also obtained from the evolution of the enstrophy, as shown in Fig. 26(b), where the maximum relative error of the enstrophy is also less than 4%.

To further measure the capability of DUGKS in capturing the small scale, the evolution of the Kolmogorov length scale is sketched in Fig. 27(a), and the results obtained by the LBE with a mesh of 256^3 are also included for comparison. As shown, the turbulent scale, from the large scale in the beginning to the smallest scale at about $t = 0.3$, can be described accurately, and the maximum relative error in the LBE results, as shown in Fig. 27(b), is less than 1.5%. This indicates that the flow

is adequately resolved by the DUGKS with the minimum $k_{\max}\eta = 3.29$. It is also found from Fig. 27(a) that due to the viscous action, the small eddies are dissipated, and the scale of the eddies becomes larger as time evolves.

Figure 28(a) shows the longitudinal and transverse correlation functions obtained from the LBE and DUGKS methods at $t = 1.95$. It can be seen that for both correlation functions, the LBE and DUGKS results agree well with each other, and the two transverse correlation functions, ρ_{22} and ρ_{33} , are identical due to the isotropic property of the Kida vortex flow.

Figure 28(b) shows the pressure-velocity correlations predicted by the LBE and DUGKS methods at $t = 1.95$. Since the Kida vortex flow considered here is incompressible, theoretically the pressure-velocity correlations defined by Eq. (35) are equal to 0. As shown in Fig. 28(b), although the values predicted by DUGKS are larger than those from the LBE method, the magnitude of the pressure velocity correlations given by both methods is on the order of 10^{-6} ,

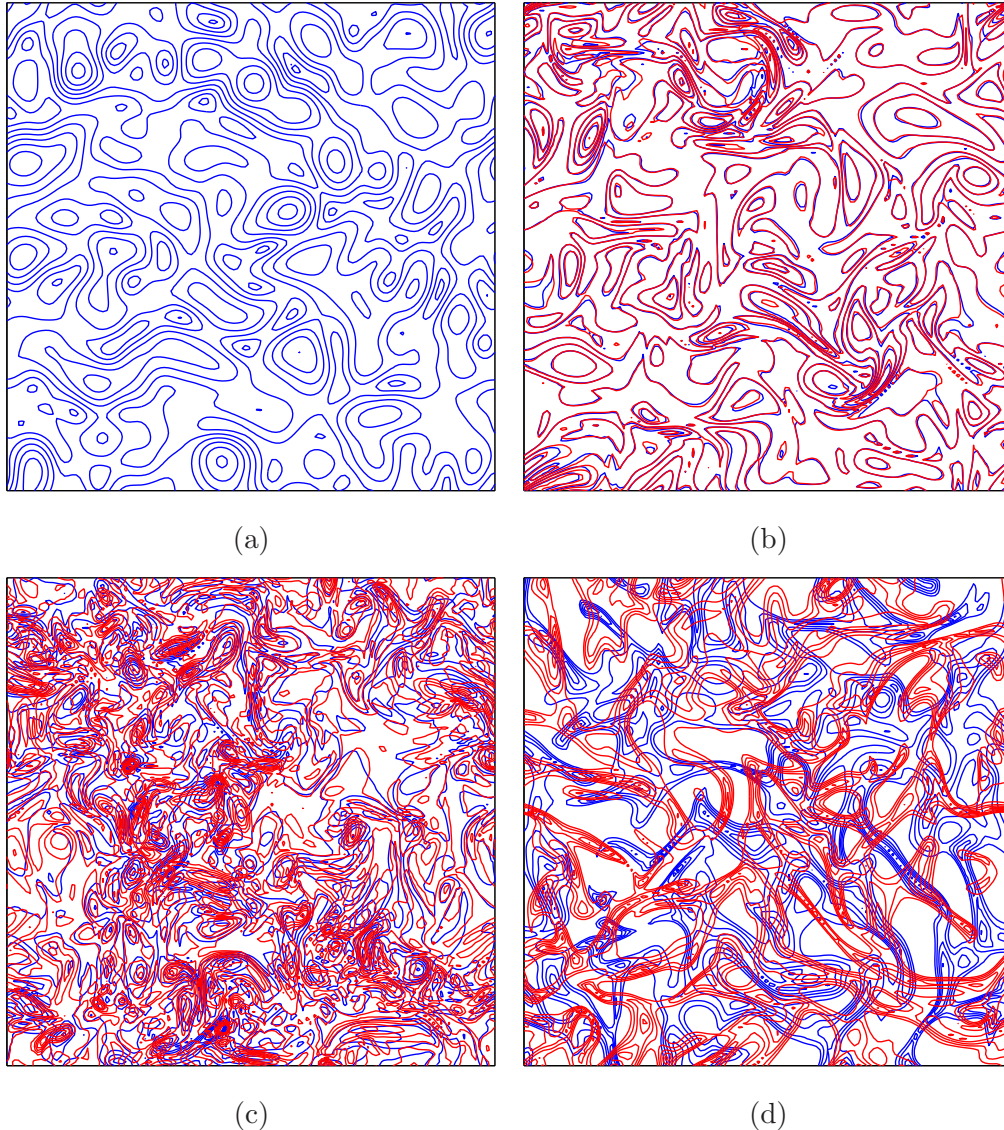


FIG. 24. Contours of normalized vorticity magnitude $\|\omega\|L/u'_0$ on the xy plane at $z = L/2$ at time (a) $t' = 0$, (b) $t' = 0.1$, (c) $t' = 0.5$, and (d) $t' = 1.5$ for $Re_\lambda = 104.24$. The solid red and blue lines denote results of the LBE and DUGKS, respectively.

which indicates that the DUGKS can accurately reproduce the incompressibility behavior.

V. DISCUSSIONS AND CONCLUSIONS

In this work, we present a comparative study of two kinetic approaches, the LBE and DUGKS methods, for direct numerical simulation of the decaying turbulent flows, including the decaying homogeneous isotropic turbulence (DHIT) and the Kida vortex flow. Although the DNS of DHIT and the Kida vortex flow are easily achievable, it is the first and essential step to validate the DUGKS method before it is used to simulate more complex turbulent flows.

In our study, we first perform the DNS of DHIT using the LBE, DUGKS, and PS methods at two mesh resolutions (128^3 and 256^3) at $Re_\lambda = 26.06$, where the minimum spatial resolution parameters $k_{\max}\eta$ are about 3.12 for the LBE and DUGKS methods and 2.07 for the PS method. In terms of

accuracy, we first compare the instantaneous flow fields. It is found that the instantaneous velocity and vorticity fields predicted by both the LBE and DUGKS methods are very similar to each other and agree reasonably well with the PS results. In addition, we compare some key statistic quantities, and we find that both methods perform an accurate prediction on all the quantities of interest due to their low numerical dissipation. We also note that the DUGKS with a coarse mesh of 128^3 underestimates the energy and dissipation rate spectra in the high-wave-number region, and yet these discrepancies vanish with a fine mesh of 256^3 . This indicates that the DUGKS has a relatively large numerical dissipation compared with the LBE method, which can be attributed to the finite-volume formulation of the DUGKS and the central difference employed in DUGKS to approximate the gradient at the cell interface. Furthermore, since the numerical viscosity ($0.5c_s^2\Delta t$) in the LBE method has been explicitly subtracted, it is not surprising that the LBE method has relatively small

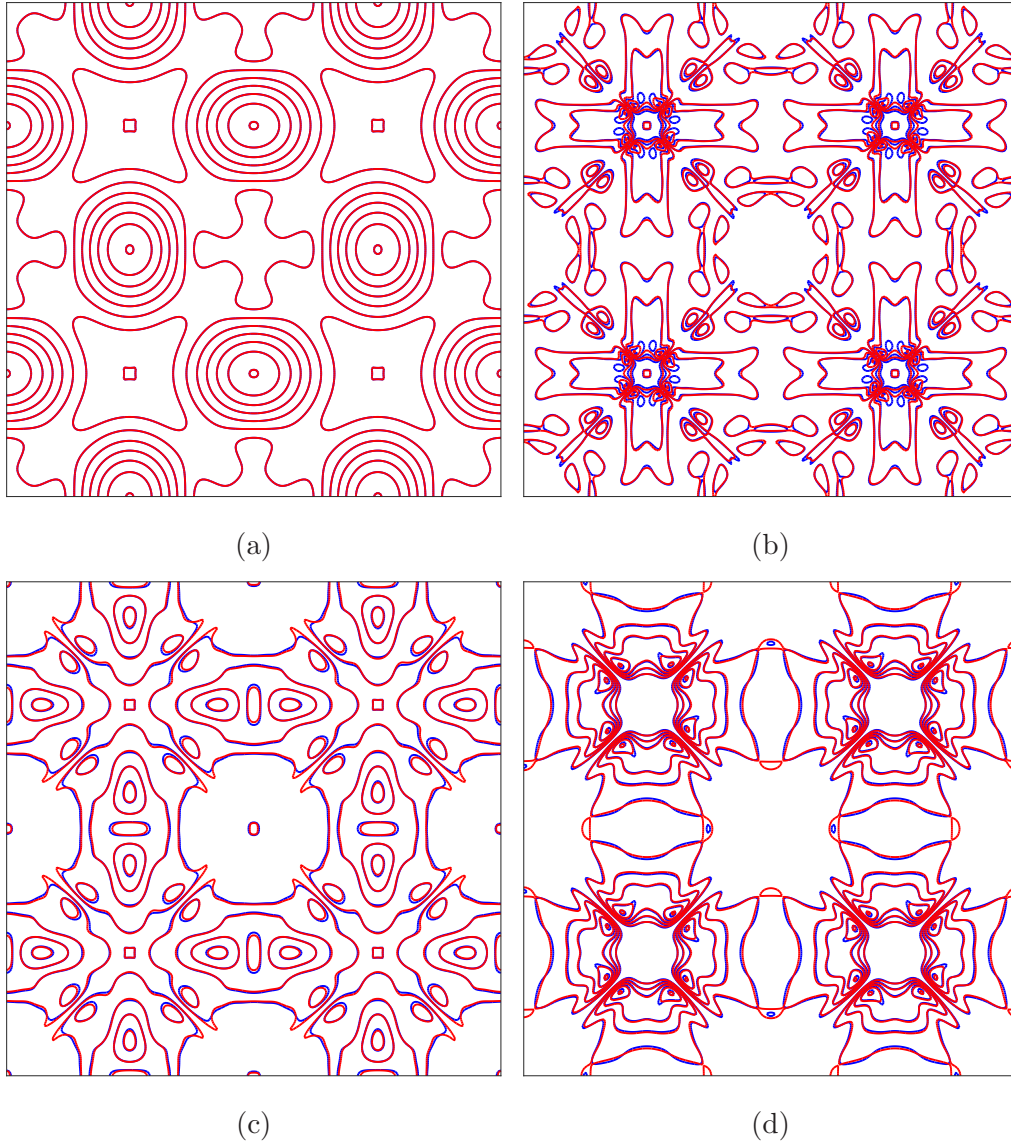


FIG. 25. Contours of the normalized vorticity magnitude $\|\omega\|L/u'_0$ on the xy plane at $z = L/2$ at time (a) $t' = 0$, (b) $t' = 0.9765$, (c) $t' = 1.9531$, and (d) $t' = 2.9297$ for $Re = 2000$ with the mesh of 256^3 . The solid blue and red lines denote results of the LBE and DUGKS, respectively.

numerical dissipation. However, as the numerical results showed, this feature has little impact on the low-order statistic quantities, and the flow can be adequately resolved by the DUGKS method with the minimum $k_{max}\eta > 3$. Moreover, we observe that the results of skewness and flatness obtained by the DUGKS have high-frequency oscillations due to the acoustic waves in the system.

The performance of the two methods at higher Reynolds numbers is also compared. Some key statistical quantities obtained by the LBE and DUGKS methods are compared with those from the PS method. The results show that good agreement is achieved between the LBE and the PS methods at both Re_λ , but there are noticeable discrepancies between the results of the DUGKS and PS methods due to the insufficient mesh resolution, which also indicates that the DUGKS is more dissipative than the LBE method.

To further evaluate the accuracy of the DUGKS, the direct numerical simulation of the Kida vortex flow is also performed with a relatively low Reynolds number, and the results are validated by those from the LBE method. The simulations are conducted with the minimum $k_{max}\eta = 3.29$, which guarantees that the results from the LBE method are adequately resolved. The results show that although DUGKS is slightly more dissipative than the LBE method, it can accurately predict the low-order statistics, such as the total energy and its dissipation rate, the enstrophy, and the longitudinal and transversal velocity correlations, and it can capture the smallest Kolmogorov length scale in turbulent flow. The results of the pressure-velocity correlation also show that the DUGKS can well reproduce the incompressibility behavior of the flow.

In terms of computational efficiency, the LBE method is about 36.8% faster than the DUGKS per time step. It should

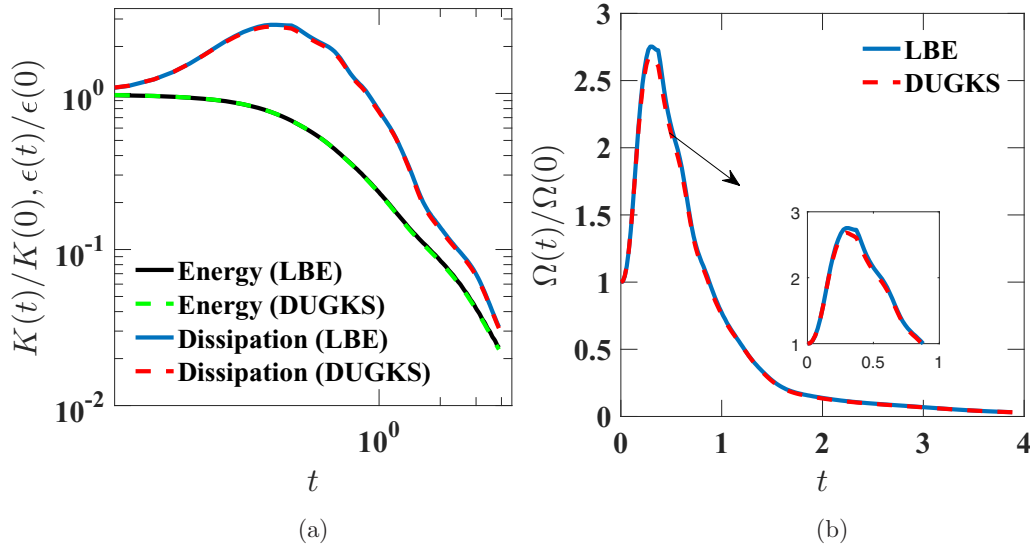


FIG. 26. Evolutions of (a) the normalized total kinetic energy K , dissipation rate ϵ , and (b) enstrophy Ω .

be noted that although the DUGKS is less efficient than the LBE method on the same uniform mesh, as a finite-volume method, the DUGKS can use nonuniform meshes without additional efforts for wall-bounded turbulence flows, such as a channel flow and pipe flow. For such flows, the mesh can be clustered near the walls where large flow gradients exist, and the computational efficiency can be largely improved, which will be presented in our subsequent work. We also assess the numerical stability of the LBE and DUGKS methods by computing the maximum stable Taylor microscale Reynolds number on a fixed mesh without considering the accuracy. The results show that the DUGKS has a better numerical stability than the LBE method, which is consistent with the previous results of laminar flows [45].

In conclusion, the LBE is less dissipative and thus more accurate than the DUGKS, but they have similar accuracy for

DNS of the decaying turbulent flows when the mesh resolution is sufficient to resolve the flow field; in addition, the DUGKS is less efficient than the LBE method with the same regular uniform mesh, but it is superior to the LBE method in terms of the numerical stability; furthermore, it is found that the DUGKS can adequately resolve the flow when the minimum spatial resolution parameter $k_{\max}\eta$ is about 3, which is a more strict requirement when compared to $k_{\max}\eta > 2$ for LBE [17] and $k_{\max}\eta > 1$ for the pseudospectral method [50]. It must be emphasized that this work is the first step toward validating the DUGKS for DNS of turbulent flows, and further tests are needed before regarding it as a viable kinetic method for DNS of turbulent flows. The main advantage of the DUGKS compared with the LBE method is that it can be implemented on nonuniform meshes easily, which we shall demonstrate in the subsequent study of wall-bounded turbulent flows.

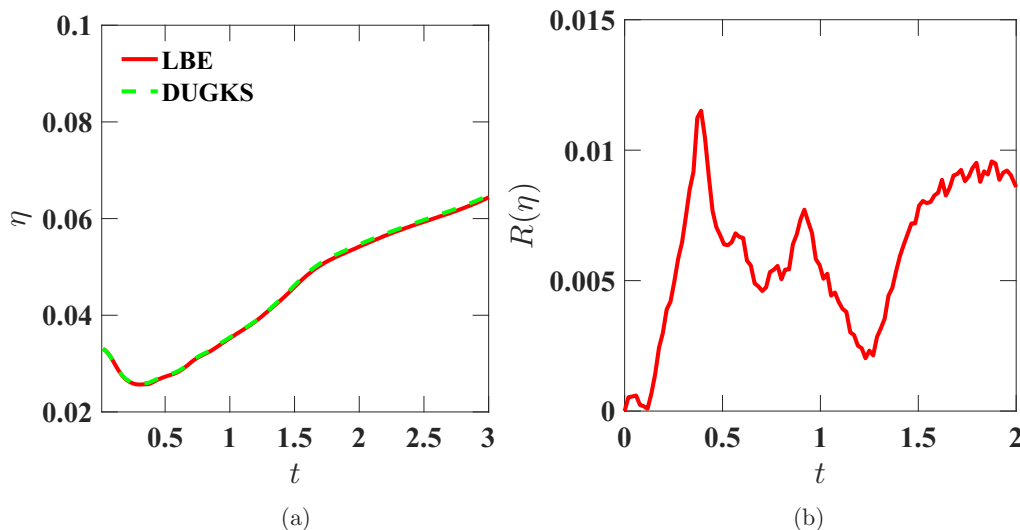


FIG. 27. Evolutions of (a) Kolmogorov length scale η and (b) the relative difference $R(\eta)$ between the results of DUGKS and LBE on the mesh of 128^3 .

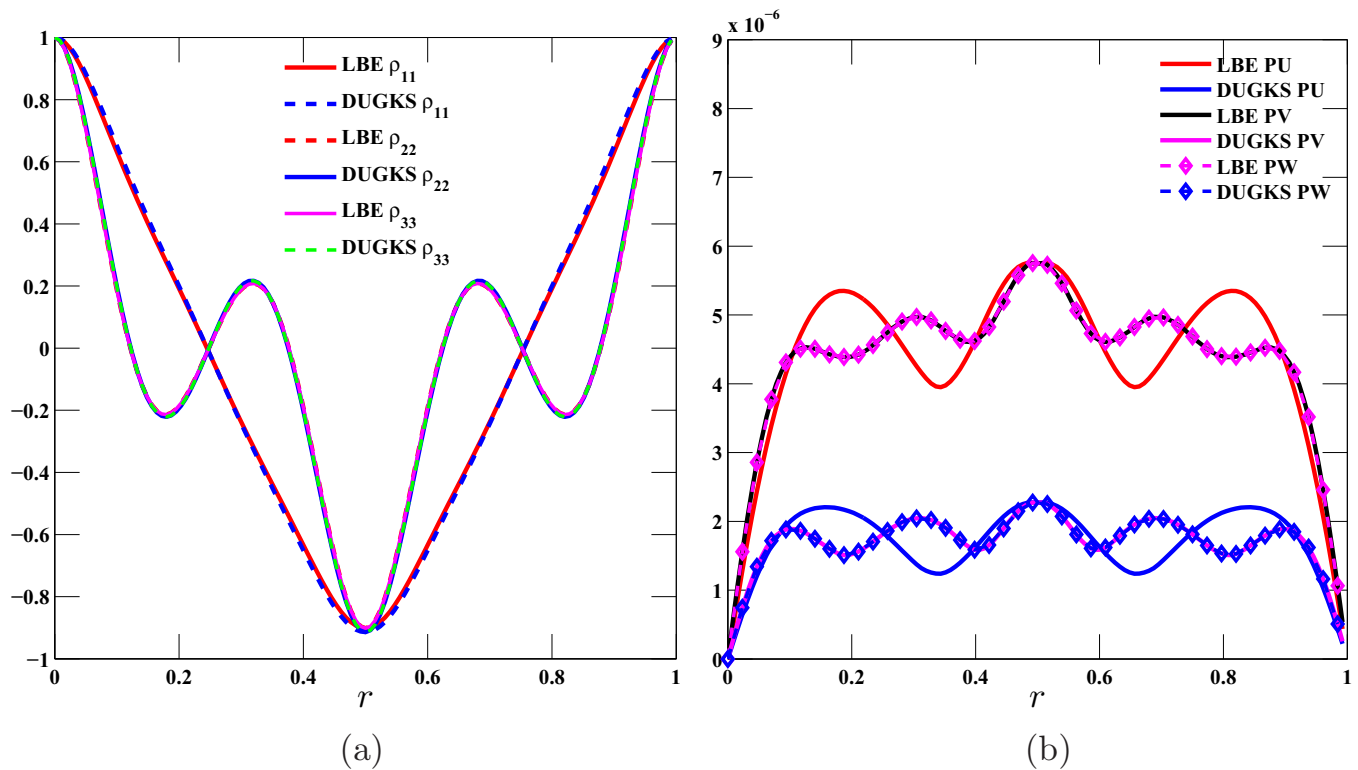


FIG. 28. Comparisons of (a) the two-point longitudinal correlation (ρ_{11}), transversal correlations (ρ_{22}, ρ_{33}), and (b) the pressure-velocity correlations (PU, PV, and PW) at $t = 1.95$.

ACKNOWLEDGMENTS

The authors acknowledge the support by the National Natural Science Foundation of China (Grant No. 51125024) and

the U.S. National Science Foundation (NSF) under Grants No. CNS1513031, No. CBET-1235974, and No. AGS-1139743.

[1] S. B. Pope, *Turbulent Flows* (Cambridge University Press, Cambridge, 2000).
 [2] H. Le, P. Moin, and J. Kim, *J. Fluid Mech.* **330**, 349 (1997).
 [3] P. Moin and K. Mahesh, *Annu. Rev. Fluid Mech.* **30**, 539 (1998).
 [4] R. D. Moser, J. Kim, and N. N. Mansour, *Phys. Fluids* **11**, 943 (1999).
 [5] B. van Leer, *AIAA Paper* **2520**, 2001 (2001).
 [6] H. Xu, W. Tao, and Y. Zhang, *Phys. Lett. A* **373**, 1368 (2009).
 [7] H. Chen, S. Kandasamy, S. Orszag, R. Shock, S. Succi, and V. Yakhot, *Science* **301**, 633 (2003).
 [8] H. Chen, S. Chen, and W. H. Matthaeus, *Phys. Rev. A* **45**, R5339 (1992).
 [9] D. O. Martinez, W. H. Matthaeus, S. Chen, and D. Montgomery, *Phys. Fluids* **6**, 1285 (1994).
 [10] S. Hou, J. Sterling, S. Chen, and G. D. Doolen, *Fields Institute Commun.* **6**, 151 (1996).
 [11] J. G. Eggels, *Int. J. Heat Fluid Flow* **17**, 307 (1996).
 [12] G. Amati, S. Succi, and R. Piva, *Int. J. Mod. Phys. C* **8**, 869 (1997).
 [13] D. d’Humières, *Philos. Trans. R. Soc. London, Ser. A* **360**, 437 (2002).
 [14] H. Yu, S. S. Girimaji, and L.-S. Luo, *J. Comput. Phys.* **209**, 599 (2005).
 [15] H. Yu, S. S. Girimaji, and L.-S. Luo, *Phys. Rev. E* **71**, 016708 (2005).
 [16] H. Yu, L.-S. Luo, and S. S. Girimaji, *Comput. Fluids* **35**, 957 (2006).
 [17] Y. Peng, W. Liao, L.-S. Luo, and L.-P. Wang, *Comput. Fluids* **39**, 568 (2010).
 [18] H. Gao, H. Li, and L.-P. Wang, *Comput. Math. Appl.* **65**, 194 (2013).
 [19] L.-P. Wang, C. Peng, Z. Guo, and Z. Yu, *Comput. Fluids* **124**, 226 (2016).
 [20] S. Chikatamarla, C. Frouzakis, I. Karlin, A. Tomboulides, and K. Boulouchos, *J. Fluid Mech.* **656**, 298 (2010).
 [21] F. Bösch, S. S. Chikatamarla, and I. V. Karlin, *Phys. Rev. E* **92**, 043309 (2015).
 [22] B. Dorschner, F. Bösch, S. Chikatamarla, K. Boulouchos, and I. Karlin, *J. Fluid Mech.* **801**, 623 (2016).
 [23] W. Liao, Y. Peng, and L.-S. Luo, *AIAA Paper* **548**, 2008 (2008).
 [24] W. Liao, Y. Peng, and L.-S. Luo, *Phys. Rev. E* **80**, 046702 (2009).
 [25] W. Liao, Y. Peng, and L.-S. Luo, *AIAA Paper* **586**, 2009 (2009).
 [26] G. Kumar, S. S. Girimaji, and J. Kerimo, *J. Comput. Phys.* **234**, 499 (2013).
 [27] M. Righi and R. Wang, in *Proceedings of the 29th International Symposium on Rarefied Gas Dynamics* (AIP, New York, 2014), Vol. 1628, p. 1363.
 [28] S. Chen and G. D. Doolen, *Annu. Rev. Fluid Mech.* **30**, 329 (1998).

- [29] S. Succi, *The Lattice-Boltzmann Equation* (Oxford University Press, Oxford, 2001).
- [30] C. K. Aidun and J. R. Clausen, *Annu. Rev. Fluid Mech.* **42**, 439 (2010).
- [31] Z. Guo and C. Shu, *Lattice Boltzmann Method and Its Applications in Engineering (Advances in Computational Fluid Dynamics)* (World Scientific, Singapore, 2013).
- [32] L.-S. Luo, M. Krafczyk, and W. Shyy, in *Encyclopedia of Aerospace Engineering*, edited by R. Blockley and W. Shyy (Wiley, New York, 2010), Chap. 56, pp. 651–660.
- [33] Z. Guo, K. Xu, and R. Wang, *Phys. Rev. E* **88**, 033305 (2013).
- [34] Z. Guo, R. Wang, and K. Xu, *Phys. Rev. E* **91**, 033313 (2015).
- [35] L. Zhu, Z. Guo, and K. Xu, *Comput. Fluids* **127**, 211 (2016).
- [36] N. Cao, S. Chen, S. Jin, and D. Martinez, *Phys. Rev. E* **55**, R21 (1997).
- [37] Z. Guo and T.-S. Zhao, *Phys. Rev. E* **67**, 066709 (2003).
- [38] G. Peng, H. Xi, C. Duncan, and S.-H. Chou, *Phys. Rev. E* **59**, 4675 (1999).
- [39] N. Rossi, S. Ubertini, G. Bella, and S. Succi, *Int. J. Numer. Methods Fluids* **49**, 619 (2005).
- [40] S. Ubertini and S. Succi, *Progr. Computat. Fluid Dynamics, Int. J.* **5**, 85 (2005).
- [41] S. Ubertini and S. Succi, *Commun. Comput. Phys.* **3**, 342 (2008).
- [42] T. Lee and C.-L. Lin, *J. Comput. Phys.* **171**, 336 (2001).
- [43] T. Ohwada, *J. Comput. Phys.* **177**, 156 (2002).
- [44] S. Chen and K. Xu, *J. Comput. Phys.* **288**, 52 (2015).
- [45] P. Wang, L. Zhu, Z. Guo, and K. Xu, *Commun. Comput. Phys.* **17**, 657 (2015).
- [46] P. L. Bhatnagar, E. P. Gross, and M. Krook, *Phys. Rev.* **94**, 511 (1954).
- [47] X. He and L.-S. Luo, *J. Stat. Phys.* **88**, 927 (1997).
- [48] B. Keating, G. Vahala, J. Yepez, M. Soe, and L. Vahala, *Phys. Rev. E* **75**, 036712 (2007).
- [49] L. Biferale, P. Gualtieri, and F. Toschi, *Phys. Fluids* **12**, 1836 (2000).
- [50] V. Eswaran and S. Pope, *Comput. Fluids* **16**, 257 (1988).
- [51] R. Mei, L.-S. Luo, P. Lallemand, and D. d’Humières, *Comput. Fluids* **35**, 855 (2006).
- [52] L. Zhu, P. Wang, and Z. Guo, [arXiv:1511.00242](https://arxiv.org/abs/1511.00242).